Open Access Articles

ChemCam results from the Shaler outcrop in Gale crater, Mars

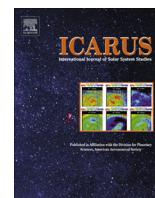|	
Citation	Anderson, R., Bridges, J. C., Williams, A., Edgar, L., Ollila, A., Williams, J., ... & Vaniman, D. (2015). ChemCam results from the Shaler outcrop in Gale Crater, Mars. Icarus, 249, 2-21. doi:10.1016/j.icarus.2014.07.025
DOI	10.1016/j.icarus.2014.07.025
Publisher	Elsevier
Version	Version of Record
Terms of Use	http://cdss.library.oregonstate.edu/sa-termsofuse

ChemCam results from the Shaler outcrop in Gale crater, Mars

Ryan Anderson [a,*], J.C. Bridges [b], A. Williams [c], L. Edgar [d], A. Ollila [e], J. Williams [e], M. Nachon [f], N. Mangold [f], M. Fisk [g], J. Schieber [h], S. Gupta [i], G. Dromart [j], R. Wiens [k], S. Le Mouélic [f], O. Forni [l,m], N. Lanza [k], A. Mezzacappa [n], V. Sautter [o], D. Blaney [p], B. Clark [q], S. Clegg [k], O. Gasnault [l,m], J. Lasue [l,m], R. Léveillé [r], E. Lewin [s], K.W. Lewis [t], S. Maurice [l,m], H. Newsom [e], S.P. Schwenzer [u], D. Vaniman [v]

[a] U.S. Geological Survey Astrogeology Science Center, 2255 N. Gemini Dr., Flagstaff, AZ 86001, USA
[b] Space Research Centre, Dept. of Physics and Astronomy, University of Leicester, Leicester LE1 7RH, UK
[c] Department of Earth and Planetary Sciences, University of California, Davis, Davis, CA 95616, USA
[d] School of Earth and Space Exploration, Arizona State University, Tempe, AZ 85287, USA
[e] University of New Mexico, Department of Earth and Planetary Sciences, Albuquerque, NM 87131, USA
[f] Laboratoire de Planétologie et Géodynamique de Nantes, CNRS, UMR6112, Université de Nantes, 44322 Nantes, France
[g] College of Earth, Ocean, and Atmospheric Sciences, Oregon State University, Corvallis, OR 97331, USA
[h] Department of Geological Sciences, Indiana University, 1001 E 10th Str., Bloomington, IN 47405, USA
[i] Department of Earth Sciences and Engineering, Imperial College London, London SW7 2AZ, UK
[j] Laboratoire de Géologie de Lyon, Université de Lyon, 69364 Lyon, France
[k] Los Alamos National Laboratory, Los Alamos, NM 87545, USA
[l] CNRS, IRAP, 9 Av. colonel Roche, BP 44346, F-31028 Toulouse cedex 4, France
[m] Université de Toulouse, UPS-OMP, IRAP, Toulouse, France
[n] Optical Science Center for Applied Research, Delaware State University, 1200 N. Dupont Highway, Dover, DE 19901, USA
[o] Museum Histoire Naturelle de Paris, 57 Rue Cuvier, 75005 Paris, France
[p] NASA Jet Propulsion Laboratory, 4800 Oak Grove Drive, Pasadena, CA 91109, USA
[q] Space Science Institute, 4750 Walnut Street, Suite 205, Boulder, CO 80301, USA
[r] Department of Natural Resource Sciences, McGill University, St-Anne-de-Bellevue, Quebec H9X 3V9, Canada
[s] ISTerre, Université Joseph Fourier, Grenoble, France
[t] Johns Hopkins University, Baltimore, MD 21218, USA
[u] Dept. of Physical Sciences, Open University, Milton Keynes LE1 7RH, UK
[v] Planetary Science Institute, 1700 East Fort Lowell, Suite 106, Tucson, AZ 85719, USA

ARTICLE INFO

ABSTRACT

The ChemCam campaign at the fluvial sedimentary outcrop "Shaler" resulted in observations of 28 non-soil targets, 26 of which included active laser induced breakdown spectroscopy (LIBS), and all of which included Remote Micro-Imager (RMI) images. The Shaler outcrop can be divided into seven facies based on grain size, texture, color, resistance to erosion, and sedimentary structures. The ChemCam observations cover Facies 3 through 7. For all targets, the majority of the grains were below the limit of the RMI resolution, but many targets had a portion of resolvable grains coarser than ~0.5 mm. The Shaler facies show significant scatter in LIBS spectra and compositions from point to point, but several key compositional trends are apparent, most notably in the average K_2O content of the observed facies. Facies 3 is lower in K_2O than the other facies and is similar in composition to the "snake," a clastic dike that occurs lower in the Yellowknife Bay stratigraphic section. Facies 7 is enriched in K_2O relative to the other facies and shows some compositional and textural similarities to float rocks near Yellowknife Bay. The remaining facies (4, 5, and 6) are similar in composition to the Sheepbed and Gillespie Lake members, although the Shaler facies have slightly elevated K_2O and FeO_T. Several analysis points within Shaler suggest the presence of feldspars, though these points have excess FeO_T which suggests the presence of Fe oxide cement or inclusions. The majority of LIBS analyses have compositions which indicate that they

are mixtures of pyroxene and feldspar. The Shaler feldspathic compositions are more alkaline than typical feldspars from shergottites, suggesting an alkaline basaltic source region, particularly for the K_2O-enriched Facies 7. Apart from possible iron-oxide cement, there is little evidence for chemical alteration at Shaler, although calcium-sulfate veins comparable to those observed lower in the stratigraphic section are present. The differing compositions, and inferred provenances at Shaler, suggest compositionally heterogeneous terrain in the Gale crater rim and surroundings, and intermittent periods of deposition.

1. Introduction

The *Curiosity* rover landed on the floor of Gale crater (137.7°E, 5.44°S) in a region that has been described as "hummocky" based on orbital mapping (Anderson and Bell, 2010; Grotzinger et al., 2013; Rice et al., 2013). Sporadic rock outcrops in the vicinity of the landing site comprise sedimentary conglomerate deposits which have been interpreted as evidence of ancient fluvial activity (Williams et al., 2013). Upon landing, the Mars Science Laboratory (MSL) science team decided to drive east toward a location named "Glenelg" where three geologic units observed from orbit converged (Grotzinger et al., 2013). The three units are the hummocky plains, a distinctive heavily cratered surface, and a light-toned, fractured unit inferred to be the distal facies of the alluvial fan that occupies much of the Curiosity landing site (Anderson and Bell, 2010; Palucis et al., 2013).

Outcrops of the light-toned, fractured unit nearest to Glenelg, informally named "Yellowknife Bay," are roughly 18 m lower in elevation than the rover's initial landing location. The lowest ~4 m of the section are composed of (in descending order) the Glenelg, Gillespie Lake, and Sheepbed members (Grotzinger et al., 2013). The Sheepbed member is a smectite-bearing mudstone with elemental composition similar to the average martian crust (Grotzinger et al., 2013; McLennan et al., 2013; Vaniman et al., 2013). The Gillespie Lake member is ~2.0 m thick and comprises a poorly sorted sandstone that overlies the Sheepbed member, and is interpreted as a distal fluvial sandstone (Grotzinger et al., 2013). It has a composition similar to the Sheepbed mudstone (McLennan et al., 2013). Overlying Gillespie Lake is the Glenelg member, which is composed of the Point Lake, Shaler, Rocknest, and Bathurst outcrops. Point Lake is characterized by pervasive cm-scale voids (Grotzinger et al., 2013), and Rocknest is characterized by fine-grained well-cemented rocks with high iron content (Blaney et al., 2014). Bathurst is a fine-grained layered rock with elevated K_2O (Grotzinger et al., 2013; Mangold et al., submitted for publication).

The "Shaler" outcrop is located at 137.4488°E 4.5905°S (planetocentric), near the location in the Glenelg region where the three distinct terrain types meet. Shaler was first identified in panoramic images from the Rocknest aeolian drift. From this distance (~40 m), it stood out as a unique thinly layered outcrop of resistant and recessive strata (Fig. 1), and due to its appearance it received the name "Shaler". The outcrop is approximately 0.7 m thick and >20 m long, and consists of well-exposed cross-stratified sandstones with significant variation in erosional-resistance, resulting in interstratification of resistant pebbly sandstones and recessive intervals. Curiosity first encountered the Shaler outcrop on sol 120 of the mission, during the descent into Yellowknife Bay, when it was analyzed only briefly by ChemCam and Mastcam.

After the science campaign in Yellowknife Bay was completed, Curiosity followed a path back up onto the hummocky plains and once again passed near Shaler. Given the interesting sedimentary structures in the Shaler outcrop, the Curiosity science team decided to conduct a more detailed investigation of Shaler on sols 309–324.

Because of the rugged nature of the exposed beds and the limited time available to analyze the outcrop, arm contact science was only possible from one rover location. However, the ChemCam instrument can analyze targets from a distance (<7 m) to determine their chemistry (Maurice et al., 2012; Wiens et al., 2012), and the Remote Micro-Imager (RMI) provides images that permit detailed analysis of target grain sizes and fine-scale sedimentary structures. The remote measurement capabilities of ChemCam were invaluable in the geologic triage at Shaler.

Here we use the results from the ChemCam campaign at Shaler to investigate sedimentary textures, examine the chemostratigraphy of the outcrop, and evaluate the composition and diagenetic history of the sedimentary facies that comprise Shaler. Detailed description of the sedimentology and stratigraphy of Shaler, and an interpretation of the sedimentary processes and paleoenvironments are presented elsewhere (Edgar et al., submitted for publication).

Note that all target and unit names used in this manuscript are informal names assigned by the *Curiosity* science team.

2. Methods and data

The ChemCam instrument (Maurice et al., 2012; Wiens et al., 2012) collects both spectroscopic and image data. ChemCam acquired data from a total of 28 non-soil targets at Shaler, 26 of which included active laser-induced breakdown spectroscopy (LIBS) plus context RMI imagery, and 2 of which were imaged with the RMI without accompanying LIBS spectra. Table 1 summarizes the ChemCam observations at Shaler, including the average ChemCam compositions in wt.%, and Figs. 1 and 2 show the locations of ChemCam targets in context on Mastcam (Malin et al., 2010) and Navcam (Maki et al., 2012) mosaics of the outcrop.

2.1. LIBS data

ChemCam LIBS uses a pulsed laser to ablate small spots (350–550 μm diameter) on targets up to ~7 m from the rover. The light emitted by the ablated plasma spark is collected by the same telescope used to transmit the laser beam, and is passed to three spectrometers which record the atomic emission spectrum over the ultraviolet (UV: 240.1–342.2 nm), violet (VIS: 382.1–469.3 nm), and visible to near-infrared (VNIR: 474.0–906.5 nm) ranges (Wiens et al., 2012).

A typical ChemCam LIBS observation involves the analysis of multiple locations on the target, with 30 laser pulses per location. For each laser pulse, a LIBS spectrum is collected. The repeated laser pulses are useful for removing dust (typically in the first several pulses) and identifying variations in composition as the laser ablates progressively deeper into the target. Average LIBS spectra for each point exclude the first 5 points to minimize the influence of dust. Surface dust on rocks is almost always removed after ~5 laser shots, see e.g. Fig. 14 of Ollila et al. (2013) and Fig. S4 of Stolper et al. (2013). The number of shots, number of locations, and the geometry of the analysis locations are all customizable
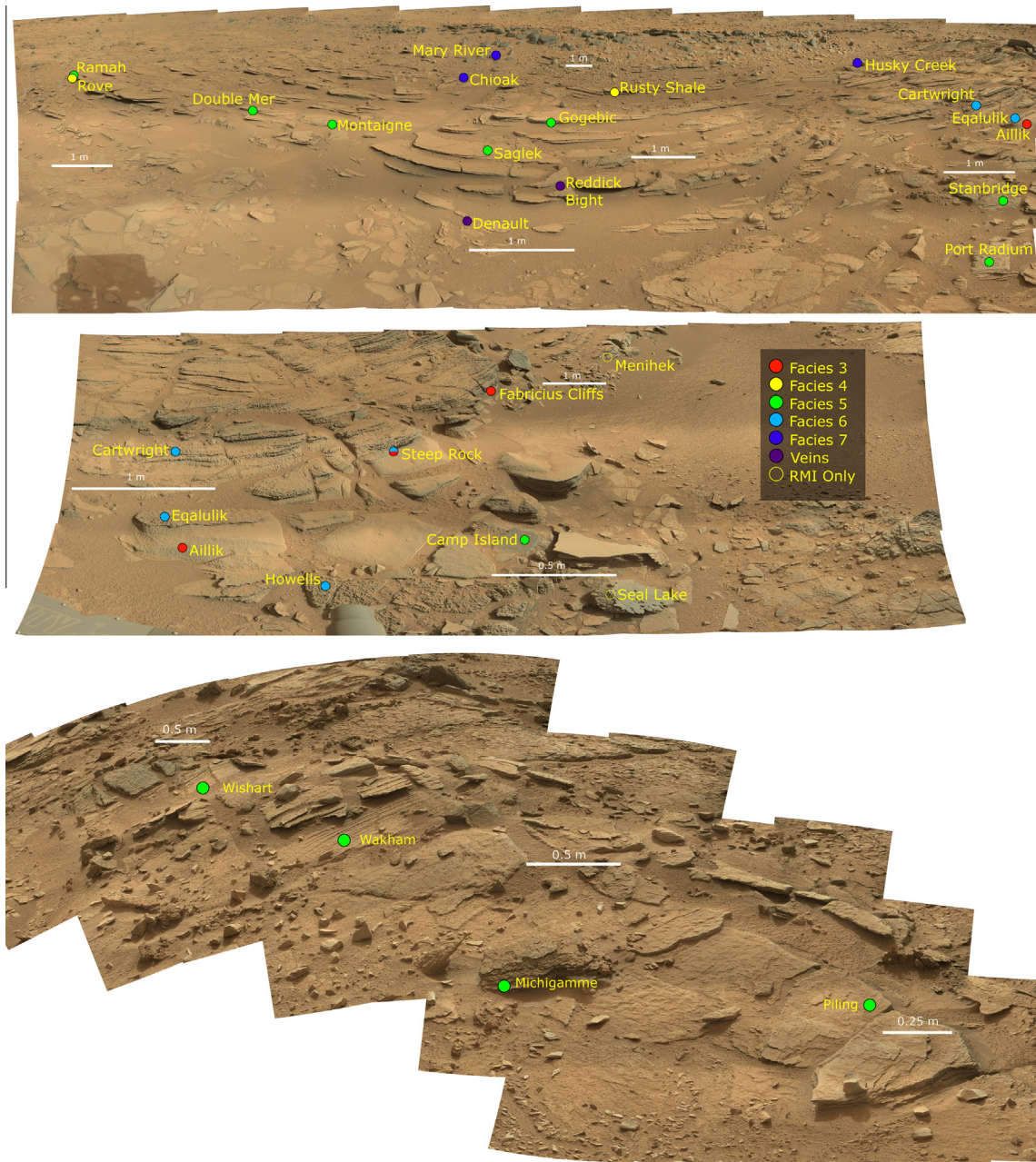
Fig. 1. Mastcam mosaics showing ChemCam targets analyzed at Shaler. (a) Sol 120 post-drive left-eye mosaic (mcam00753), (b) Sol 317 post-drive left-eye mosaic of Shaler contact science area (mcam01300), (c) Sol 311 right-eye mosaic of Shaler (mcam01279). Mosaics were made by merging calibrated images using the free open-source Hugin software (http://hugin.sourceforge.net/).

depending on the science intent of the observation. Common geometries for LIBS observations are square grids (e.g. 3 × 3, 4 × 4) and vertical or horizontal lines (e.g. 1 × 5, 10 × 1).

2.2. RMI data

In addition to LIBS spectra, ChemCam also collects images using the RMI. The RMI has a pixel scale of 19.6 μrad per pixel and produces 1024 × 1024 pixel images with a circular field of view of 20 mrad (Le Mouélic et al., 2015). Image data are restricted to a circle inscribed in the square array, and the RMI is co-aligned with the LIBS laser such that the laser spot is very close to the center of the image. For all LIBS observations, at least 2 RMI images are acquired: one before and one after LIBS. For observations that span a wider area, additional RMI images are interspersed between LIBS

analyses to ensure complete RMI coverage of the analyzed area. These images are useful for interpreting LIBS results by providing morphological/textural context for the spectroscopic data.

The RMI can also be used independent of LIBS to collect high-resolution images of targets of interest. By operating independently, the RMI can image targets beyond the maximum LIBS range as well as in the "restriction zone" from 1.94 to 2.22 m where the number of LIBS shots is restricted because of the potential to damage the telescope's secondary mirror (Maurice et al., 2012). Like the LIBS measurements, RMI observations are customizable, allowing multiple images to be acquired at offset positions to produce an RMI mosaic, or multiple images of the same location at different focus settings to produce a combined "z-stack" image with optimum focus in all parts of the image (Le Mouélic et al., 2015). Z-stacks are particularly useful for images that would normally

Table 1
Summary of ChemCam targets at Shaler, with average compositions in wt.%.

Sol	Target	Sequence	Facies	Distance	Obs. type	SiO$_2$	TiO$_2$	Al$_2$O$_3$	FeO$_T$	MgO	CaO	Na$_2$O	K$_2$O	Total
319	Aillik	ccam01319	3	2.46	3 × 3	41.8	0.9	5.8	17.9	6.4	7.0	2.1	0.0	81.9
319	Menihek	ccam03319	3	5.16	3 × 3	45.0	0.8	6.9	20.3	5.7	6.4	2.4	0.1	87.6
322	Fabricius_cliffs	ccam02322	3	3.93	5 × 1	44.4	1.0	7.1	19.2	5.5	7.6	2.2	0.2	87.2
309	Rove	ccam01309	4	3.79	20 × 1	44.3	1.1	7.0	18.4	6.2	6.3	2.0	0.6	85.9
316	Rusty_Shale	ccam01316	4	4.67	10 × 1	51.6	1.1	8.8	20.4	5.2	5.9	3.0	1.2	97.2
121	Stanbridge	ccam01121	5	3.9	1 × 5	47.3	0.8	6.6	18.1	7.5	5.7	2.2	0.4	88.6
121	Port_Radium	ccam02121	5	3.13	1 × 5	44.7	1.1	7.2	17.5	5.4	6.0	2.0	0.6	84.6
121	Port_Radium_2	ccam03121	5	3.17	RMI only									
309	Ramah	ccam02309	5	3.77	5 × 1	47.5	0.8	7.9	17.2	5.0	6.0	2.1	1.4	88.0
311	Michigamme	ccam01311	5	4.07	1 × 20	48.0	1.0	8.2	18.1	5.4	7.0	2.3	1.0	90.9
311	Wakham_Bay	ccam04311	5	5.45	1 × 20	49.8	0.9	8.4	19.1	5.5	6.4	2.9	1.2	94.1
311	Piling	ccam05311	5	3.91	3 × 3	42.3	0.8	6.7	19.1	4.5	5.8	2.0	0.4	81.7
312	Wishart	ccam01312	5	6.23	1 × 5	50.1	0.9	8.1	19.6	7.5	5.6	3.0	1.0	95.7
315	Gogebic	ccam02315	5	3.3	3 × 3	46.0	1.2	7.3	17.7	6.2	8.0	2.1	0.5	88.9
315	Saglek	ccam03315	5	2.47	3 × 3	43.7	1.0	7.9	16.1	4.1	6.9	2.0	0.6	82.3
317	Montaigne	ccam01317	5	2.26	4 × 4	43.7	1.2	7.0	17.8	5.1	6.1	1.8	0.5	83.3
317	Double_mer	ccam02317	5	2.79	3 × 3	50.0	0.9	7.0	19.3	6.4	5.1	2.1	0.9	91.7
323	Camp_Island	ccam03323	5	2.3	5 × 1	44.8	0.9	7.8	17.4	3.9	8.1	2.6	1.0	86.6
323	Seal_Lake	ccam01323	5 + 6	2.11	RMI only									
319	Eqalulik	ccam02319	6	2.64	3 × 3	46.1	1.0	7.4	17.7	5.3	6.9	2.2	0.3	86.9
319	Cartwright	ccam04319	6	3.11	1 × 6	45.6	1.0	8.0	17.5	4.8	7.5	2.2	0.5	87.1
323	Steep_Rock	ccam02323	6 + 3	3.02	1 × 20	45.8	1.0	8.0	18.8	4.3	7.1	2.4	0.7	88.0
324	Howells	ccam01324	6	2.27	5 × 5	46.0	1.2	8.1	17.8	3.8	6.5	1.9	0.9	86.2
315	Chioak	ccam01315	7	4.592	3 × 3	52.2	1.0	9.6	19.9	4.3	6.2	3.1	1.4	97.8
316	Mary_River	ccam04316	7	6.1	3 × 3	54.0	1.0	10.1	19.2	5.8	6.9	3.4	1.7	101.9
322	Husky_creek	ccam01322	7	6.07	4 × 4	Low signal to noise								
316	Reddick_Bight	ccam03316	Vein/Soil	2.73	3 × 3	32.6	0.5	6.1	10.5	6.8	18.3	1.9	0.2	76.8
317	Denault	ccam03317	Vein/Soil	2.3	1 × 10	36.9	1.0	7.5	13.4	5.5	9.8	1.9	0.2	76.2
					RMSE:	7.1	0.6	3.7	4	3	3.3	0.7	0.9	

be limited by the narrow depth of field of a single image, such as rough or distant targets. RMI mosaics in this paper were produced by merging calibrated, flat-field-corrected RMI images using the free open-source software Hugin (http://hugin.sourceforge.net/). Z-stacks were produced using Heliconfocus commercial software.

2.3. RMI analysis methods

To aid in the characterization of the Shaler outcrop facies, we conducted a survey of grain sizes using RMI mosaics. The RMI has the highest angular resolution of the mast-mounted cameras on Curiosity (~50 μrad; Langevin et al., 2013; Le Mouélic et al., 2015). However, the narrow depth of focus (~1 cm at 2 m distance; Le Mouélic et al., 2015) limits grain resolution outside of the best focus field in the mosaics.

Each target was evaluated by determining the grain size and percent area distribution of the resolvable grains. To determine the scale of each image, we used the known pixel scale (θ) of the RMI (19.6 μrad) and the distance to the target (d) to calculate the size of a pixel (x) at that distance: $x = d \tan \theta$. In most cases, the distances recorded for each RMI in a mosaic are slightly different (average difference ~3 cm, maximum difference 23.6 cm for Wakham_Bay), so the pixel scale is calculated using an average of these distances. Grain size and area were measured using the NIH software package ImageJ. Grain size was determined by measuring the longest axis of every visible grain in the mosaic, which may underestimate grain size if the grain is oriented such that the long axis is not visible (Yingst et al., 2013). Grain sizes were binned according to the Wentworth scale (Wentworth, 1922) (pebble = 4–64 mm, granule = 2–4 mm, very coarse sand = 1–2 mm, coarse sand = 0.5–1 mm).

Percent area distribution of the resolvable grains was determined in each RMI mosaic by measuring the area of all resolvable grains in a ~1000 mm^2 area. Due to the narrow RMI depth of focus, mosaics frequently contained out-of focus regions where accurate grain analyses were not possible. To accurately estimate the percent area distribution, each 1000 mm^2 area was centered on an in-focus region with measurable grains. In mosaics where multiple areas were in-focus and contained measureable grains (e.g. Wakham_Bay and Michigamme), the 1000 mm^2 area was centered on the region with the greatest density of resolved grains. The percent area calculations varied by ~1% when the 1000 mm^2 area was placed in other in-focus regions, so no significant bias in the measurements appears to result from centering on the highest concentration of resolved grains. In targets Fabricius_Cliffs, Camp Island, and Eqalulik, the total area over which the grains were measured was smaller due to the target in the RMI mosaic being smaller than 1000 mm^2.

One consideration when measuring grain sizes is erratic grain size frequencies for small grains. Grain edges can be blurred due to pixelation and grains smaller than the pixel size are unresolvable (Friday et al., 2013). Previous studies have shown that 2-D grain analysis overestimates particle size in small grains (35–140 μm/pixel; Fedo et al., 2012). To mitigate this problem, we followed the approach of Yingst et al. (2008) and required all measurable grains be composed of at least 5 pixels. Each target's resolution is determined by the distance to the target; therefore we calculated the maximum unresolved grain size (in micrometers) that could be composed of 5 pixels in all of the targets. Maximum unresolved sizes in most targets were ⩽0.5 mm (except for Wishart, at 0.578 mm). Although some targets had a small number of measureable grains smaller than 0.5 mm, this size is close to the limit of resolution for most targets, and some grains of this size may have been missed. Therefore, we assigned 0.5 mm (lower coarse sand boundary) as the cut off for measured grains in RMI mosaics at Shaler.

2.4. LIBS analysis methods

We use two related methods of qualitatively comparing ChemCam spectra: Principal Components Analysis (PCA) and
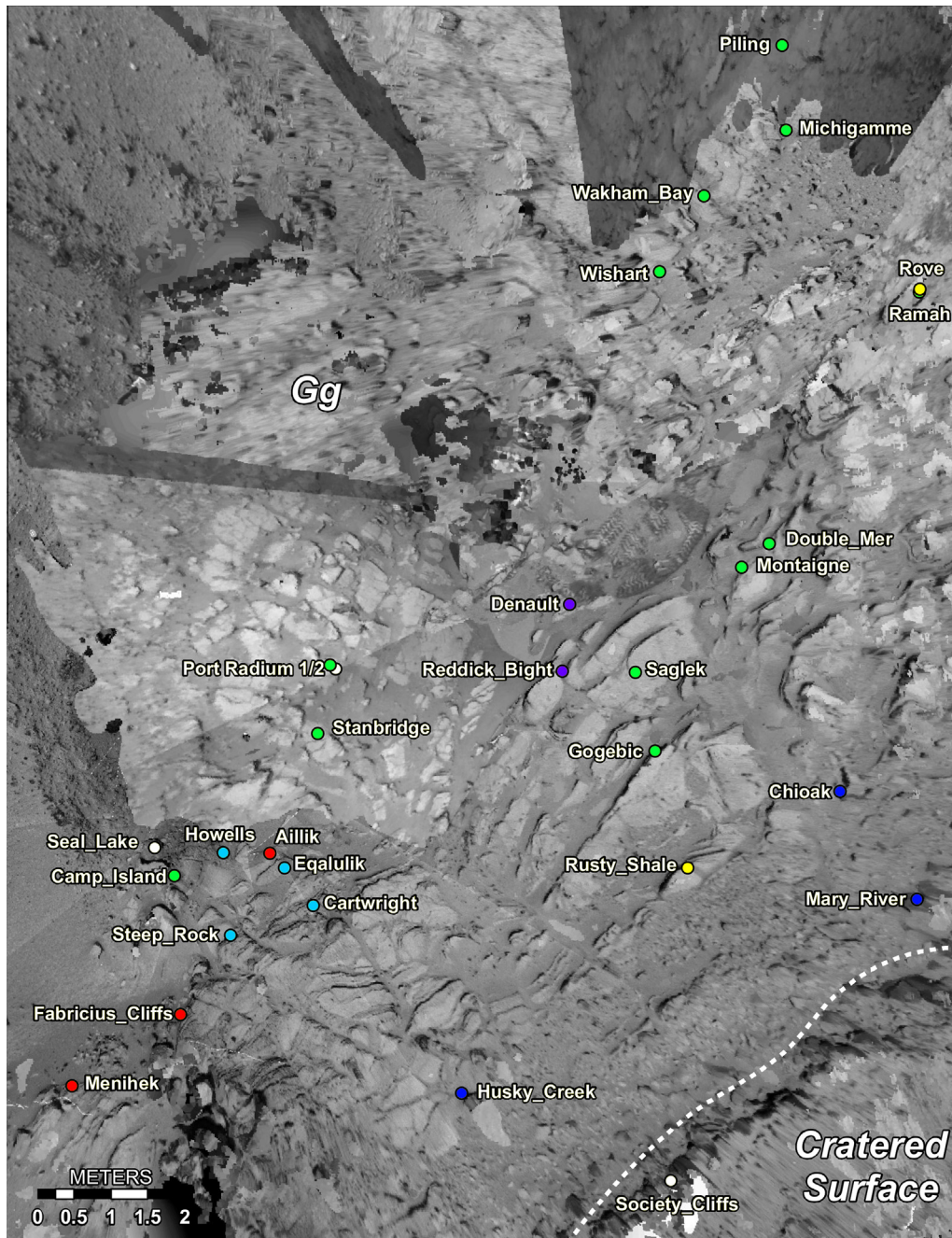
Fig. 2. Overhead Navcam view of the Shaler outcrop, with points color-coded by facies (see key in Fig. 1). "Gg" stands for "Glenelg member". North is toward the top of the page (this figure adapted from McLennan et al., 2013, Fig. S7). (For interpretation of the references to color in this figure legend, the reader is referred to the web version of this article.)

Independent Components Analysis (ICA). With PCA (Jolliffe, 2002) we try to simplify multivariate data sets by decomposing them into multiple orthogonal components. With ICA we do not impose orthogonality and instead try to minimize the statistical dependence between components (Comon, 1992). Both methods produce "scores," which are linear combinations of the original wavelengths, weighted by "loading" vectors. The loading vectors for PCA and ICA of LIBS spectra have an appearance similar to spectra when plotted against wavelength, with strong peaks corresponding to larger weights per pixel on specific atomic emission lines. Spectra with emission lines that match strongly positive loadings will tend to have higher scores, while spectra with emission lines that have negative loadings will have lower scores.

For ICA, independent components identified by the algorithm can be obtained that correspond to a single element, resulting in scores that are a qualitative measurement of the strength of that element's emission lines in the spectrum (Forni et al., 2013). PCA loadings indicate the directions of largest variance in the data set and tend to contain a combination of negative and positive correlations with emission lines from most major elements. Thus, when PCA scores are plotted they do not correspond to single elements, but they serve as a good visualization of the variation in the dataset.

Chemical compositions are determined from LIBS spectra using a partial-least-squares (PLS) model. PLS is a multivariate method related to PCA that searches for a set of components that

simultaneously decompose both the LIBS spectra and the compositions and explains the covariance between them (Abdi, 2003). This is accomplished using a "training set" of spectra from samples for which the true composition is known. The resulting model can be used to predict the composition of an unknown target based on its spectrum, assuming the unknown material is within the range of compositions in the training set. For this study, a variant of PLS called PLS1 was used, meaning that a separate model was trained and optimized for each of the major element oxides rather than using a single model to predict all oxides at once (Clegg et al., 2009; Rosipal and Krämer, 2006).

The accuracy of compositions measured with PLS1 is expressed in terms of root mean squared error of cross-validation (RMSE). RMSE is calculated using leave-one-out cross validation with the training set of known geostandards. Each standard is removed from the training set, a PLS1 model is generated using the remaining standards, and the composition of the removed standard is then predicted. This process is iterated until all standards have been left out and predicted with the remaining standards. Leave-one-out cross validation provides a conservative estimate of the accuracy of the model based on the full training set when analyzing targets of unknown composition. The RMSEs for each of the major elements are given in Table 1, based on a spectral training set taken on 69 standards with the ChemCam flight model prior to launch (Wiens et al., 2013). Work is underway to improve the accuracy by expanding the training set and improving the calibration steps (Clegg et al., 2014). For the calculations of average facies composition in this paper, average spectra that yield a major element total greater than 110.1 wt.% (100% plus the quadrature sum of the RMSE values for each major element), are rejected. Only two of the analysis points at Shaler were rejected for this reason. In general points with such high totals tend to have high SiO_2, Al_2O_3, and alkali elements. Results from the target Husky_Creek (Facies 7) were also excluded based on low signal to noise.

The precision of PLS1 LIBS predictions is significantly better than the absolute accuracy, as demonstrated by Blaney et al. (in press). For this reason, much of the analysis in this paper is based on compositions that have been normalized to the average ChemCam composition of the Sheepbed mudstone, following the methods of Mangold et al. (submitted for publication). By normalizing to Sheepbed, systematic errors in the ChemCam quantitative results should be minimized. Sheepbed was chosen as the normalizing composition because it is very fine-grained, homogeneous, and was analyzed extensively by both ChemCam (Mangold et al. (submitted for publication)) and APXS (McLennan et al., 2013). In assessing the similarity between observations at Shaler and those collected on other units or target types encountered by the rover, we used the target classifications of Mangold et al. (submitted for publication).

3. Shaler facies

The Shaler outcrop can be subdivided into seven facies based on grain size, resistance to erosion, texture, color, and sedimentary structures (Edgar et al., 2014). Each facies represents a distinct sedimentary process or environment. While facies were initially identified using Mastcam images, additional details such as grain size and stratification were revealed by MAHLI and ChemCam RMI images. Five of the seven facies were investigated by ChemCam (Figs. 1, 2 and 4; Table 1), and we provide a brief description and discussion of grain size measurements for each. A more detailed description of the facies and sedimentology of Shaler will be presented in (Edgar et al., 2014).

Facies 1 and Facies 2 are defined by (Edgar et al., 2014) as "fine-grained convoluted" and "fine-grained evenly laminated sandstone," respectively. However, because these facies were not recognized in images until after the rover had left the outcrop, there are no ChemCam observations of either one.

Facies 3 is mostly seen at the southwestern end of the Shaler outcrop (Figs. 1 and 2) and is generally smooth with a uniform appearance, although faint cross-bedding is visible. It is interpreted to have formed from migration of fluvial dunes, possibly isolated in a paleo-depression (Edgar et al., 2014). In at least one location, this facies contains light-toned fracture fill, thought to be a calcium sulfate vein similar to those observed elsewhere at Shaler, as discussed below. The observation Fabricius_Cliffs was targeted to analyze this vein, but because of its small size the LIBS analysis points missed the vein and sampled either soil or Facies 3 rock. In addition to Fabricius_Cliffs, other targets assigned to Facies 3 are Aillik, Menihek, and the bottom five points of Steep_Rock.

Facies 4 is a recessively weathering facies that is interstratified with the prominent thin resistant beds of Facies 5. Facies 4 is weathered to a knobby texture and, in some Mastcam images, vertical resistant features are present. ChemCam analyzed two examples of Facies 4 (Rove and Rusty_Shale). Rove is a paired observation with Ramah – Ramah is a resistant bed which overlies the more recessive Rove target.

The most prominent facies at Shaler is Facies 5. It is composed of cross-stratified pebbly sandstones that are relatively resistant to erosion, and are interpreted to be the result of migrating sandy bedforms (Edgar et al., 2014). In many locations, Facies 5 is interbedded with the more recessively weathering Facies 4. At least 13 of the ChemCam targets at Shaler are categorized as Facies 5 (Table 1, Figs. 1 and 2). The target Camp Island is substantially darker in appearance than most examples of Facies 5. The darker appearance of Camp Island may be the result of its orientation, allowing the wind to clear off the dust that is ubiquitous on most horizontal Facies 5 surfaces.

Facies 6 has a rough, pitted texture and is predominantly composed of unresolved (<0.5 mm) sand grains with an irregular distribution of larger (coarse to pebble-sized) grains. This facies resists erosion slightly better than Facies 3, as can be seen by comparing Eqalulik and Aillik in Fig. 1b. It tends to form rough surfaces and displays compound cross-bedding. The dark tone of Facies 6 is likely related to the surface roughness, with shadowing of pits and dust removal from small knobs both contributing to a darker tone.
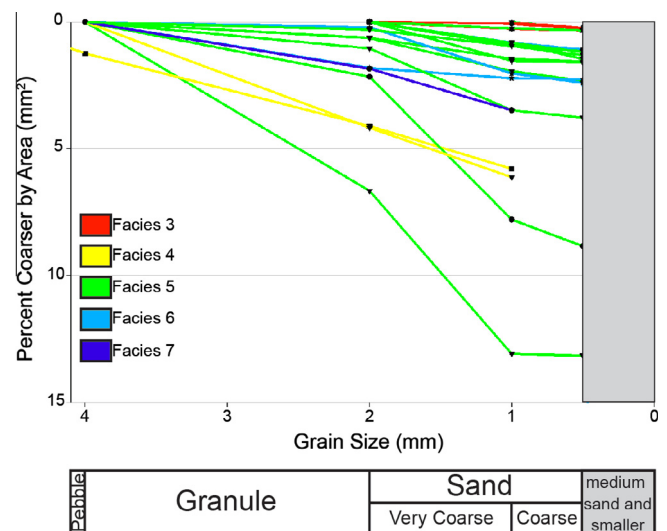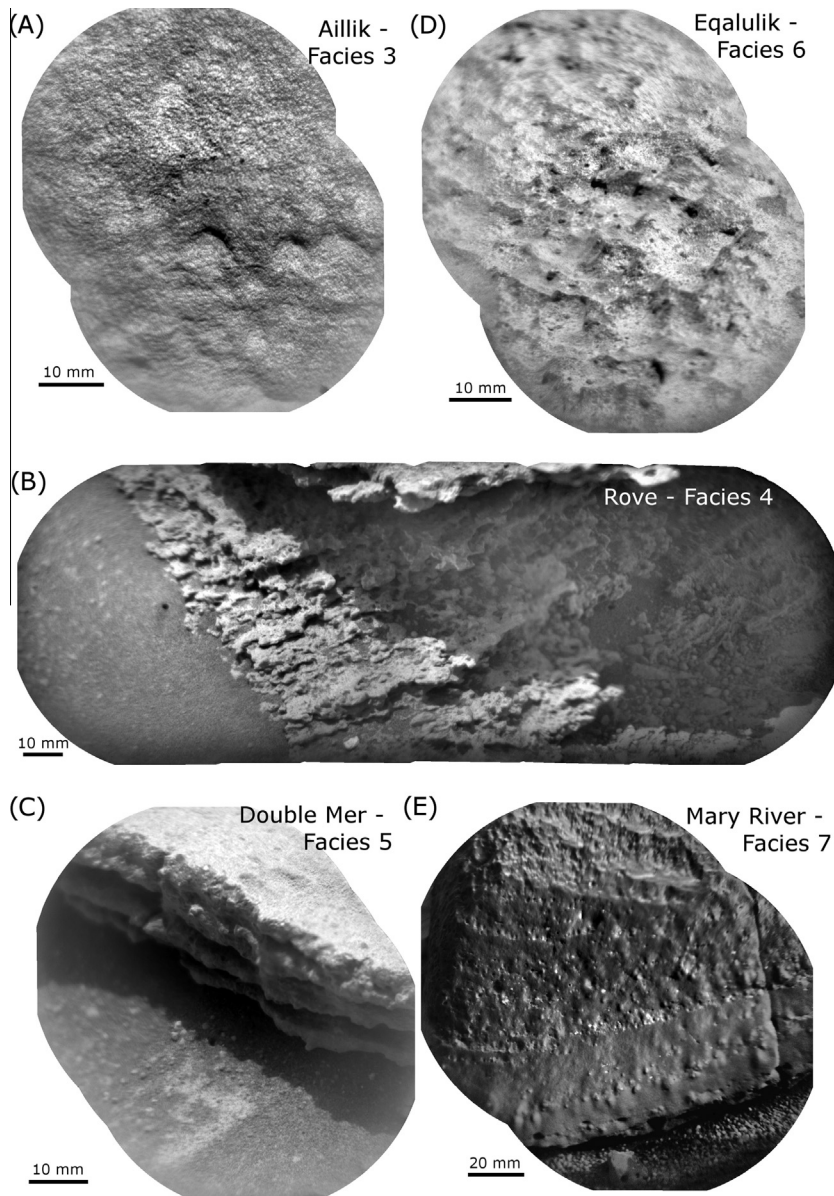

Fig. 3. Plot showing the areal fraction of each target that is coarser than each grain size. Note that most targets have less than 3% of their visible surface area that is coarser than 1 mm.

Fig. 4. RMI mosaics of representative examples of Shaler facies. (A) Aillik, an example of Facies 3. Note the uniform appearance. (B) Rove, an example of the recessive Facies 4. Neither of the ChemCam observations of this facies captured the vertical fractures seen in Mastcam. (C) Target Double_Mer is an example of Facies 5. Note the edges of resistant beds visible. The lower left half of this mosaic is soil. (D) Eqalulik, an example of the Facies 6. (E) Mary_River, an example of Facies 7. Note the dark tone and bounding surface between successive bedsets.

ChemCam targets assigned to Facies 6 are Eqalulik, Cartwright, Howells, and the upper part of Steep_Rock.

Facies 7 occurs as a resistant capping material at the top of the Shaler stratigraphy, and is characterized by its dark-tone and blocky appearance. Although many examples of this facies appear massive, with favorable lighting conditions cross-bedding is apparent, as in the ChemCam target Mary_River where a bounding surface between two bed sets is preserved (Fig. 4e). Facies 7 can be subdivided into two subfacies: one that is coarser-grained and cross-stratified (Facies 7a), and one that is finer grained and well-laminated (Facies 7b), with occasional nodules. All LIBS points on Facies 7 were on subfacies 7a.

Facies 7 forms a capping unit at the top of the Shaler outcrop that may represent the edge of the cratered surface terrain type mapped from orbit. It was also hypothesized to be related to the rocks observed at Rocknest, given the similar appearance and elevation. In addition to Mary_River, other targets assigned to Facies 7 are Chioak and Husky_Creek (low LIBS signal to noise).

4. RMI results

We measured grain sizes in 27 targets at the Shaler outcrop and applied the methodology of Yingst et al. (2008, 2013) to determine limitations on grain resolution. For all targets, the majority of the visible surface is composed of grains that are unresolvable in the RMI images (smaller than coarse sand; Fig. 3). Measurable grain sizes range from coarse sand (the smallest resolvable grain size in RMI) to pebble.

All of the Facies 3 targets had grains that were unresolvable over >99% of their visible area. However, at most 0.3% and 0.2% of grains were resolvable in RMI mosaics of Fabricius Cliffs and Menihek, respectively. These measured grains range in size from sub-coarse sand to very coarse sand. Given the large fraction of unresolved grains, the measurable grains appear to be the coarse-grained tail of the grain size distribution. Aillik was observed with the Mars Hand Lens Imager (MAHLI; Edgett et al., 2012) as well as with RMI. The MAHLI Aillik images have a

resolution of ~20.2 µm/pixel, and can therefore resolve grain diameters of 60–80 µm (~very fine sand size). However, dust on the target made it difficult to identify fine grains, and so the grains observed with MAHLI ranged from ~100 to 150 µm.

Measured grain sizes in Facies 4 range from very coarse sand to pebble, and are on average 2.37 mm (granule). Resolvable grains represent at most 6.1% of the total area on Rove, and 5.8% of the total area on Rusty_Shale. Both targets appear to be grain-supported. The presence of grains up to granule and fine pebble size in the recessive Facies 4, suggests that the recessive nature is the result of a change in the properties or abundance of cementing material rather than a decrease in average grain size.

The targets in Facies 5 also have a significant fraction of unresolvable grains (smaller than coarse sand) in the RMI images (between 87% and 100% unresolved, Fig. 3). There is no measurable variation in grain size corresponding to the lamination in Facies 5. Measurable grain sizes range from coarse sand to pebble, and are on average 1.29 mm (very coarse sand).

The grains in Facies 6 are also mostly unresolved in RMIs, with both Eqalulik and the upper portion of Steep_Rock having only 1.1% and 1.2% of their visible area composed of measureable grains, respectively. Howells and Cartwright are 2.2% resolvable and 2.4% resolvable, respectively. Despite the large fraction of unresolved grains, those that are resolved in Facies 6 range up to pebble-size. The presence of pebble-sized grains in a target that is otherwise finer than coarse sand suggests that Eqalulik is poorly sorted. MAHLI also observed Eqalulik, and can resolve grains 60–80 µm in diameter (~very fine sand size). In MAHLI images of Eqalulik, measurable grains were ~100–335 µm. Measurable grain sizes in Facies 6 range from coarse sand to pebble, and are on average 1.35 mm (very coarse sand). Of the Facies 7 targets, only Mary_River contained resolvable in-place grains, which ranged from very coarse sand to granule, and are on average 1.945 mm in size (very coarse sand). The resolvable grains in Mary_River compose at most 3.5% of the target area. All Chioak grains are sub-coarse, based on comparison with resolvable coarse sand and larger grains in the nearby soil. No grains in Husky_Creek were resolvable and no soil grains were present in the RMI. The grains are therefore assumed to be sub-coarse based on its similar appearance to Chioak.

In addition to the 5 facies analyzed by ChemCam, two ChemCam observations hit light-toned veins: Reddick_Bight and Denault. These two targets are not assigned to a facies because they are partially obscured by soil, so it is difficult to distinguish between soil and outcrop grains. However, material surrounding the vein in RMI images of Reddick_Bight appears to have the same knobby texture as the recessive, vertically-fractured Facies 4. A third observation, Fabricius_Cliffs, targeted a light-toned vein within Facies 3, but the vein was very small and the points analyzed by LIBS were on the host rock instead of the vein.

The target Seal_Lake, for which there are only RMI images, consists of a thin fine-grained erosion-resistant bed overlying a rougher, less-resistant portion. No grains are resolvable in Seal_Lake (grain size <0.5 mm) and no soil grains were present. The fine grained nature and distinctive appearance of Seal_Lake may indicate that it should be assigned to a separate facies.

5. LIBS results

5.1. Qualitative results (PCA and ICA)

In general, within each facies there is significant heterogeneity from point to point, as shown on a PCA scores plot in Fig. 5. For ease of comparison between the different facies, all ICA and PCA plots are shown as both scatterplots and simplified outlines of the points for each facies. The cloud of Shaler points spans a significant portion of the full range of spectral diversity observed by the Curiosity rover through sol 360. There is considerable overlap between the different Shaler facies, indicating that the variation within a given facies is generally greater than the variation between facies.

Several points stand out as spectrally distinct from the rest of Shaler in Fig. 5. Those with high positive values in component 1 and low positive values in component 2 are the high-Ca light toned veins analyzed at targets Denault and Reddick_Bight. The other group of outlying points plots down and to the right of the main cluster, indicating elevated Si, Al, Na, and K. These points stand out even more from the rest of Shaler in a plot of the ICA scores for the Al and Si components (Fig. 6a and b).

Fig. 6c and d show an ICA plot of the K and Na components. Although there is still considerable overlap between the facies, for a given value in the Na component, Facies 3 plots with a lower value in the K component and Facies 7 plots with higher K. This separation in K is also seen in the quantitative results, as discussed below.

Fig. 6e and f show an ICA plot of the Mg and Fe components. The Shaler facies are not clearly distinguishable from one another in this plot, but they are clearly distinct from the rocks at Rocknest, plotted in black. The Rocknest points show a significantly stronger Fe signal and a weaker Mg signal.

The high-Ca points at Reddick Bight and Denault are quite prominent in ICA plots as well (Fig. 6g and h), with very high Ca component scores. As the strength of the Ca scores increases, the H component scores also increase slightly. However, the strongest hydrogen signature in the Shaler observations comes from points that hit soil, indicating that the sulfate veins are only slightly hydrated. The points with the highest Ca scores also have low Si scores, consistent with a Ca-sulfate composition.

Fig. 7 shows Reddick Bight and Denault RMIs and spectra from locations 5 and 8 on Reddick Bight and location 4 on Denault. The RMIs show that these points analyzed light-toned veins, similar to those observed elsewhere in Yellowknife Bay (Nachon et al., 2014). In addition to intense Ca lines, the spectra from these points exhibit sulfur lines, an element usually difficult to identify using LIBS. In the laboratory under terrestrial conditions, electronically excited sulfur in the plasma of sulfur-bearing samples has been shown to react with oxygen, limiting detection of sulfur (Dudragne and Amouroux, 1998). Detection of sulfur has been shown to be easier in a Mars atmosphere than in the Earth's atmosphere (Sallé et al., 2004; Sobron et al., 2012), and compositionally similar light-toned veins observed by ChemCam also show sulfur lines (Nachon et al., 2014). Other elements that could potentially serve as anions linked to Ca have been investigated, but no better fit than S was found (Nachon et al., 2014). Fig. 7 also shows that the spectra of the putative Ca-sulfate points had detectable hydrogen emission. The level of H emission observed is similar to that seen by ChemCam in loose soils on Mars. Thus, the Ca-sulfate veins in Shaler may be weakly hydrated.

6. Quantitative results and discussion

6.1. Average compositions

Table 2 lists the average ChemCam composition for each of the Shaler facies, as well as the major stratigraphic units at Yellowknife Bay (YKB): the Sheepbed member, Gillespie Lake member, and the Point Lake, Rocknest, and Bathurst outcrops. The "Snake" – a clastic dike that cuts the Sheepbed and Gillespie members (Grotzinger et al., 2013) – is also listed. For these average unit compositions, spectra with low signal to noise and those that appear to have
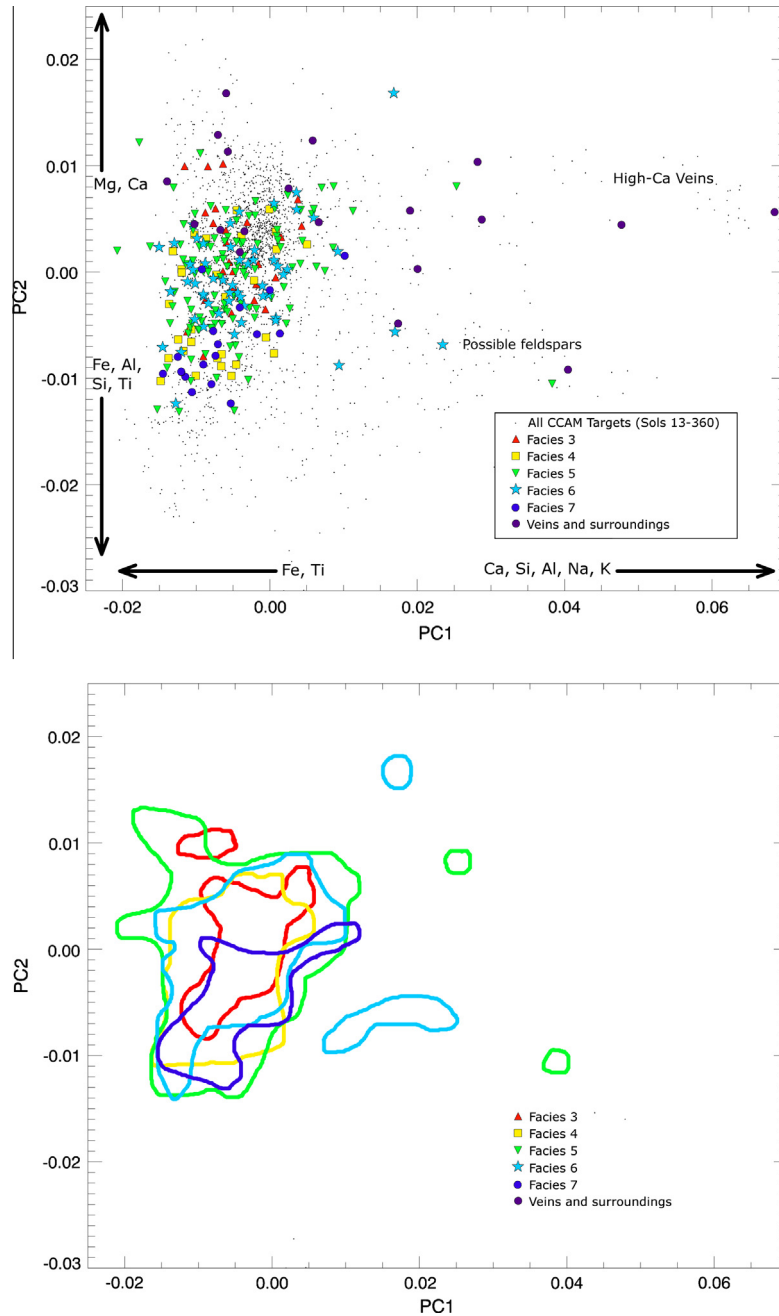
Fig. 5. PCA scores for ChemCam targets through Sol 360. Shaler points are separated into facies as indicated by the key. Each point represents the average of all ChemCam laser shots at that location (typically 30 shots).

sampled diagenetic features (e.g. raised ridges, light-toned veins) are excluded. Points that hit soil instead of the intended target are also excluded. McLennan et al. (2013) and Mangold et al. (submitted for publication) present detailed descriptions and discussion of the chemical stratigraphy at Yellowknife Bay

Fig. 8 shows the average compositions of the Shaler facies, normalized to the compositions of the Sheepbed member. This normalization allows all of the major elements to be plotted on the same scale, removes any systematic errors in the PLS accuracy, and emphasizes relative rather than absolute differences in composition. We therefore do not represent the RMSE for each element on this and similar plots. RMSE and absolute compositions are listed in Tables 1 and 2. The error bars in Figs. 8 and 9 are the standard deviation of the normalized compositions that were averaged

for each facies. This serves as an estimate of the heterogeneity of the points.

Fig. 8 shows that Facies 3 and Facies 7 have the most distinctive compositions, while the remaining facies are generally similar. Facies 3 has very low K_2O (0.2 wt.%) compared to Sheepbed (0.5 wt.%). Facies 7 has elevated K_2O (1.5 wt.%), Na_2O (3.2 wt.%), Al_2O_3 (9.7 wt.%), and SiO_2 (52.5 wt.%). Given the greater distance of the Facies 7 targets compared to other facies (Table 1), we investigated the possibility that the distinctive composition of Facies 7 was a distance effect. We applied a distance correction based on Melikechi et al. (2014) to the spectra for Mary_River and Chioak and calculated the composition using the corrected spectra. The differences in average Facies 7 composition (corrected results minus uncorrected results) were −3.8 wt.% SiO_2, 0.3 wt.% TiO_2,
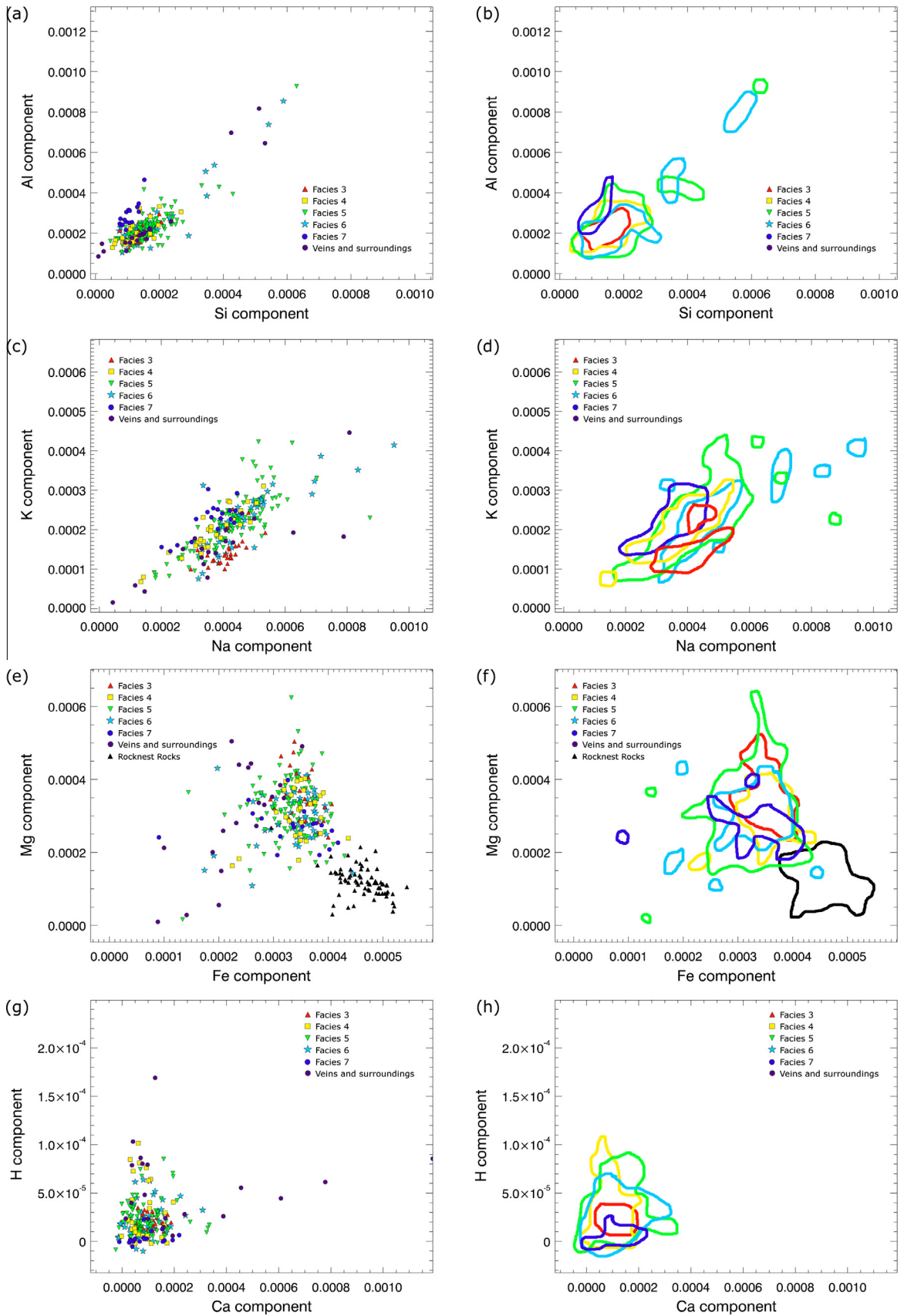
Fig. 6. ICA sores plots, and corresponding simplified facies outlines for ease of comparison. (a and b) Al vs. Si components. Note that a small number of points have elevated Al and Si signals in their spectra. These are interpreted as locations with feldspars within the LIBS spot. (c and d) K vs. Na components. Note that Facies 3 and Facies 7 have similar Na values to other Shaler facies, but are differentiated in the K component. (e and f) Mg vs. Fe component. Notice that Rocknest rocks (black) are clearly distinct from Shaler. (g and h) H vs. Ca component. High Ca points are Ca-sulfate veins. High H points are soils.
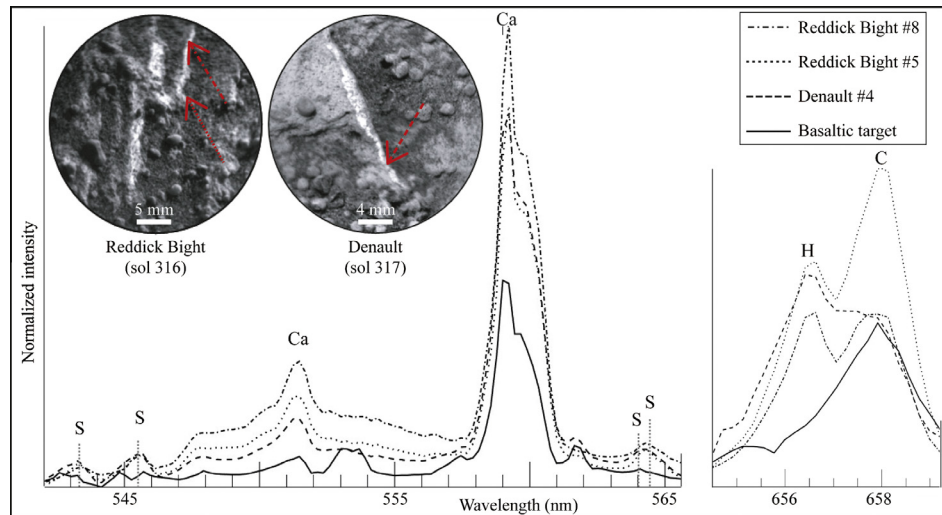
Fig. 7. ChemCam spectra of the locations 5 and 8 on Reddick Bight, and location 4 on Denault show sulfur lines in addition to intense calcium lines and hydrogen. Carbon lines are from excitation of the atmosphere. Image insets show RMI of the two targets, with the sulfur-bearing locations (arrows). The amplitude of the emission lines has been normalized to the portions of the spectra shown. For reference, a spectrum from the norite calibration target is also plotted.

Table 2
Average composition (wt.%) of Shaler facies and selected units, outcrops, and targets.

Name	Unit/outcrop[a]	# of points	SiO$_2$	TiO$_2$	Al$_2$O$_3$	FeO$_T$	MgO	CaO	Na$_2$O	K$_2$O	Total
Facies 3	Shaler	27	43.7	0.9	6.7	19.1	5.7	7.0	2.2	0.2	85.5
Facies 4	Shaler	28	46.7	1.1	7.7	19.2	5.9	6.1	2.4	0.9	89.9
Facies 5	Shaler	107	46.5	1.0	7.6	18.1	5.4	6.5	2.3	0.8	88.2
Facies 6	Shaler	55	46.0	1.1	8.0	18.0	4.3	6.8	2.2	0.7	87.0
Facies 7	Shaler	18	52.5	1.0	9.7	19.3	5.5	6.9	3.2	1.5	99.5
Sheepbed		527	45.7	1.1	8.0	16.7	6.1	6.5	2.3	0.5	86.9
Gillespie Lake		106	45.7	1.1	7.7	17.6	6.4	6.0	2.2	0.3	87.0
Point Lake		105	46.6	1.0	8.4	17.8	3.5	6.5	2.5	0.9	87.1
Rocknest rocks		110	51.5	1.3	7.4	20.7	1.3	5.1	1.9	0.9	90.0
Snake		23	45.8	0.9	7.3	18.1	4.9	5.3	2.3	0.1	84.7
Bathurst		5	46.6	1.50	7.4	18.0	7.6	5.8	1.9	1.1	89.9
Knob_Lake	Point Lake	8	52.0	1.0	10.5	19.0	2.9	5.9	3.0	1.4	95.6
Chantrey	Float	25	49.3	1.3	8.5	19.3	6.4	5.9	2.4	1.2	94.2
Jackson_Lake[b]	Float	19	48.0	1.2	8.1	18.0	6.6	6.3	2.3	1.1	91.6
Kasegalik	Float	5	56.6	1.3	9.8	18.2	6.8	5.0	2.9	2.0	102.4
Jake_Matijevic[c]	Float	14	57.0	0.9	10.0	16.3	2.0	6.5	3.3	1.3	97.4
Post_Hill	Float	8	55.0	0.8	9.8	15.2	2.6	6.3	3.0	1.5	94.2
Kiwi_Lake	Float	9	49.6	1.5	8.8	20.2	6.8	6.0	2.6	1.2	96.7
Black_Trout	Float	8	59.4	1.0	10.8	16.0	1.8	6.0	3.1	1.4	99.5
	RMSE:		7.1	0.55	3.7	4	3	3.3	0.7	0.9	

RMSE = Root mean squared error of cross validation, an estimate of accuracy.
[a] Unit/Outcrop designation based on Mangold et al. (submitted for publication).
[b] Average of Jackson_Lake, Jackson_Lake_2, and Jackson_Lake_3.
[c] Average of Jake and Jake_Matijevic.

−0.5 wt.% Al$_2$O$_3$, −0.3 wt.% FeO$_T$, 0.7 wt.% MgO, 0.1 wt.% CaO, −0.1 wt.% Na$_2$O, and −0.2 wt.% for K$_2$O. These differences were small enough that we interpret the distinctive composition of Facies 7 as a real difference in the rocks. Therefore, for the following discussion we used the un-corrected results to simplify the comparison with the other facies.

To identify units and targets with similar compositions to the Shaler facies, we quantified the similarity between compositions using Euclidean distance in the eight dimensional space defined by the major element oxides. Prior to calculating this distance, the compositions were standardized by subtracting the mean of each major element and dividing by the standard deviation. This normalization step prevents more abundant elements (e.g. SiO$_2$) from dominating the distance measure. Then we calculated the average composition for each of the major stratigraphic units or outcrops in the YKB sequence, and the average composition for each ChemCam LIBS target. The distance between the average standardized composition for each Shaler facies and the average standardized composition for each unit and target can then be used to identify similarities.

Using this method, Facies 3 is found to be most similar in composition to the "Snake," a clastic dike that cuts through the Sheepbed and Gillespie members (Grotzinger et al., 2013). After the Snake, Gillespie and Sheepbed are the closest in average composition to Facies 3, but they do not have the very low K$_2$O observed in Facies 3 and the Snake. The similarity in these compositions is shown in Fig. 9a, and absolute values are in Table 2.

Using the simple distance metric, the "unit" with the most similar composition to Facies 7 is the average of the rocks classified as "float" by Mangold et al. (submitted for publication). The most
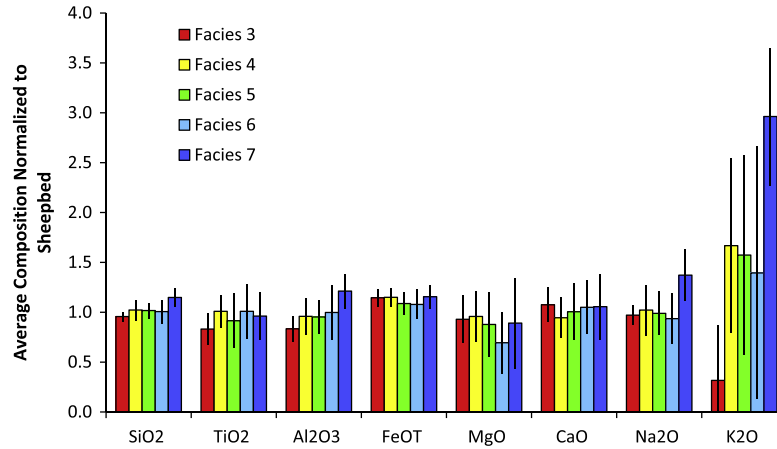
Fig. 8. Average composition of the Shaler facies, normalized to Sheepbed mudstone. Error bars are the standard deviation of normalized compositions and primarily reflect the heterogeneity of the targets within each facies.
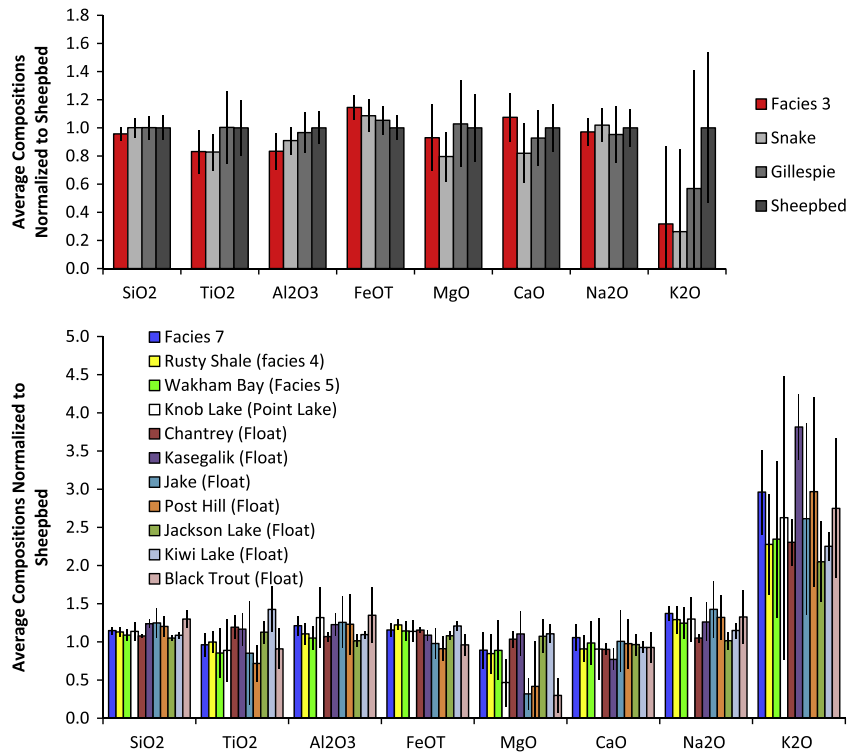
Fig. 9. (a) Facies 3 is similar in composition to the "Snake," and somewhat similar to Gillespie and Sheepbed, although they do not have as low K$_2$O. (b) Targets with average K$_2$O > 1.0 wt.%, at least 5 analysis points with good results, and overall similar compositions to Facies 7. Similarity decreases from left to right. The targets include other Shaler targets (Rusty Shale, Wakham_Bay), a Point Lake target (Knob_Lake), and multiple float rocks. Error bars are standard deviation of the compositions and primarily reflect target heterogeneity.

similar in-place stratigraphic unit is Point Lake, despite its significantly lower K$_2$O content (0.86 wt.%). Because the average composition of the float rocks was similar to Facies 7, we investigated individual targets using the distance metric, excluding targets with fewer than 5 "good" analysis points, where "good" means that the laser hit the intended rock and the total of the major elements did not exceed 110.1 wt.%. Additionally, to ensure that identified targets with similar compositions to Facies 7 shared the trait of high K$_2$O, we added a constraint, excluding any targets with average K$_2$O content of less than 1.0 wt.%.

Using these constraints to consider individual targets rather than units, the target most similar in composition to Facies 7 is Rusty Shale, one of the two Shaler targets in Facies 4. Table 1 shows that Rusty Shale and Rove, the other target in Facies 4, are quite

different in composition with higher SiO$_2$, FeO$_T$ and K$_2$O in Rusty Shale. Wakham_Bay, part of Facies 5, also shows a somewhat similar average composition to Facies 7. If the requirement for at least 5 analysis points is relaxed, Wishart (which had only four points that hit the rock) also shows a similar composition. These two targets are located close to each other on the outcrop, and are the targets from Facies 5 that are most similar in composition to Facies 7. This may indicate variation in composition across Facies 5. Knob_Lake, a Point Lake target, is among the targets closest in composition to Facies 7, though it is very heterogeneous, with three points that are significantly higher in SiO$_2$ and alkalis pushing the average composition toward high K$_2$O.

The rest of the 10 targets closest in composition to Facies 7 (with K$_2$O > 1 wt.%) are float rocks: Chantrey, Kasegalik, Jake_Matijevic,

Post_Hill, Jackson_Lake, Kiwi_Lake, and Black_Trout. Images of these rocks are compiled in Fig. 10. The rocks share some characteristics with Facies 7 including a dark tone (when not obscured by dust), blocky erosion-resistant nature, apparent layering in some cases (Chantrey, Jackson_Lake, Kasegalik, Kiwi_Lake), and a pitted texture with apparent specular reflections in other cases (Black_Trout and Post_Hill). The Facies 7 targets also show these two textures, with Chioak and Husky_Creek having pitted surfaces while Mary_River shows a smoother surface with evidence of bedding (Fig. 11). The rough and pitted float rocks generally have low MgO compared to Facies 7, and although the float rocks have $K_2O > 1$ wt.%, only Kasegalik has higher K_2O than Facies 7.

The elevated K_2O coupled with a higher K/Na ratio in many of the layered float rocks near YKB has been noted by Mangold et al. (submitted for publication), who interpreted it as evidence of a distinct source. Mangold et al. (submitted for publication) grouped the layered float rocks with Bathurst. While Bathurst does have elevated K_2O, similar to Facies 7, it has low Na_2O and high MgO and TiO_2 compared to Facies 7 (Table 2). Using the criteria described above, many of the float rocks have compositions more similar to Facies 7 than Bathurst.

6.2. Evidence of alteration

Fig. 12 shows a ternary diagram with Al_2O_3, $CaO + Na_2O + K_2O$, and $FeO_T + MgO$ at its vertices (typically called an A-CNK-FM diagram). This diagram is commonly used in sedimentary geology to assess the degree of chemical weathering observed. In terrestrial basaltic systems, progressively increasing alteration tends to shift points up and to the right as the abundance of Al_2O_3 relative to
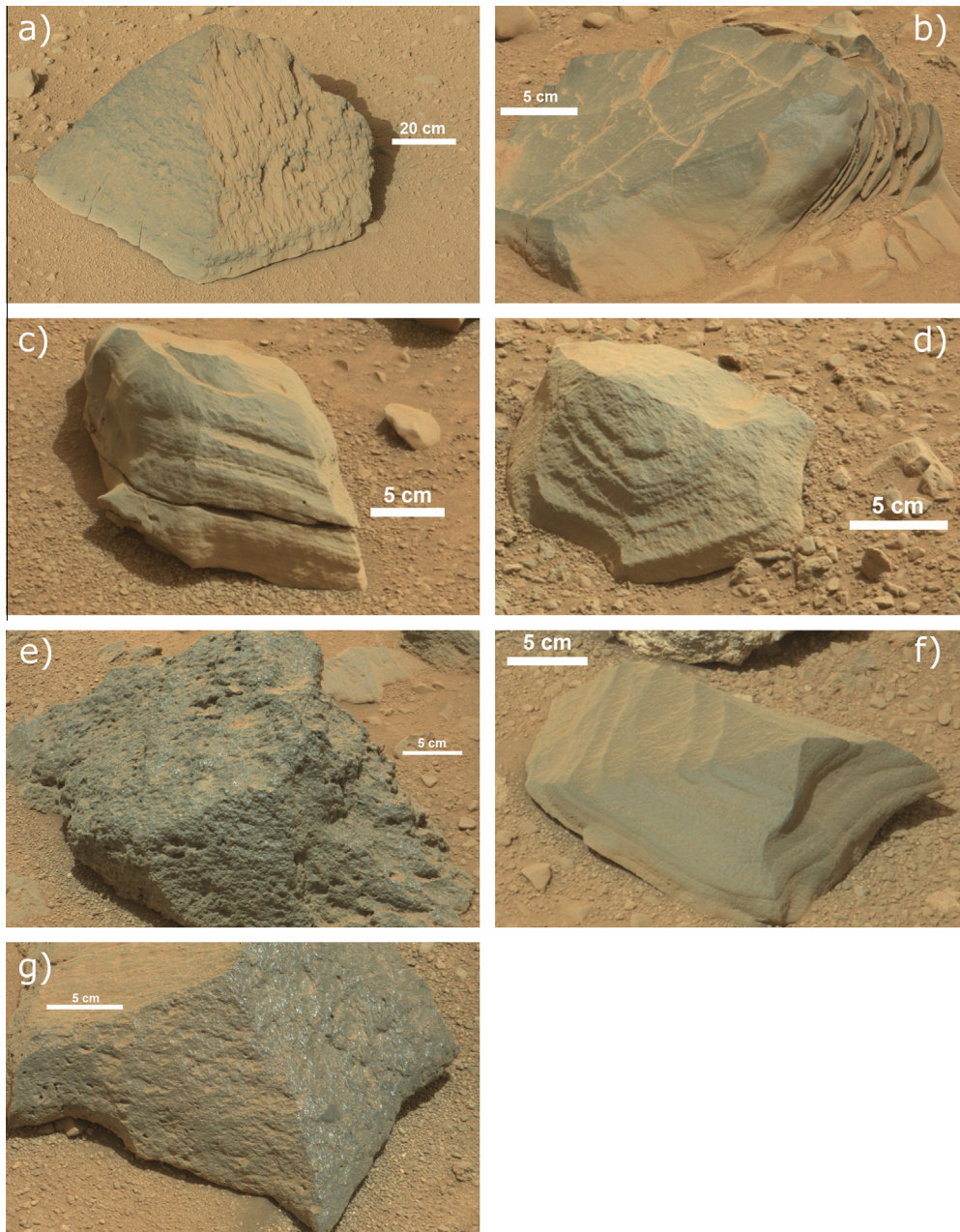

Fig. 10. Mastcam images of float rocks with $K_2O > 1$ wt.%, at least 5 good analysis points, and compositions similar to Facies 7. (a) Jake_Matijevic (Sol 44, mcam 00204), (b) Jackson_Lake (Sol 114, mcam00699), (c) Kiwi_Lake (Sol 116, mcam00733), (d) Chantrey (Sol 326, mcam01323), (e) Post_Hill (Sol 332, mcam01344), (f) Kasegalik (Sol 335, mcam01351), (g) Black_Trout (Sol 349, mcam01418).
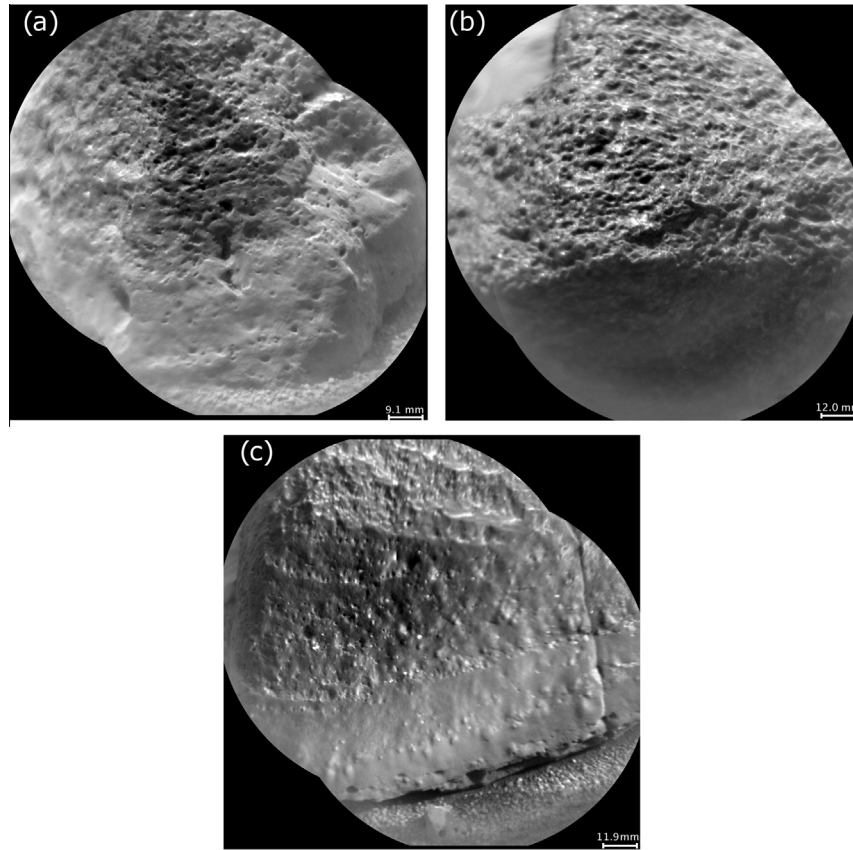
Fig. 11. RMI images of Facies 7 targets. (a) Chioak, (b) Husky_Creek, (c) Mary_River. Note the pitted texture of Chioak and Husky_Creek, and the bedding apparent in Mary_River.
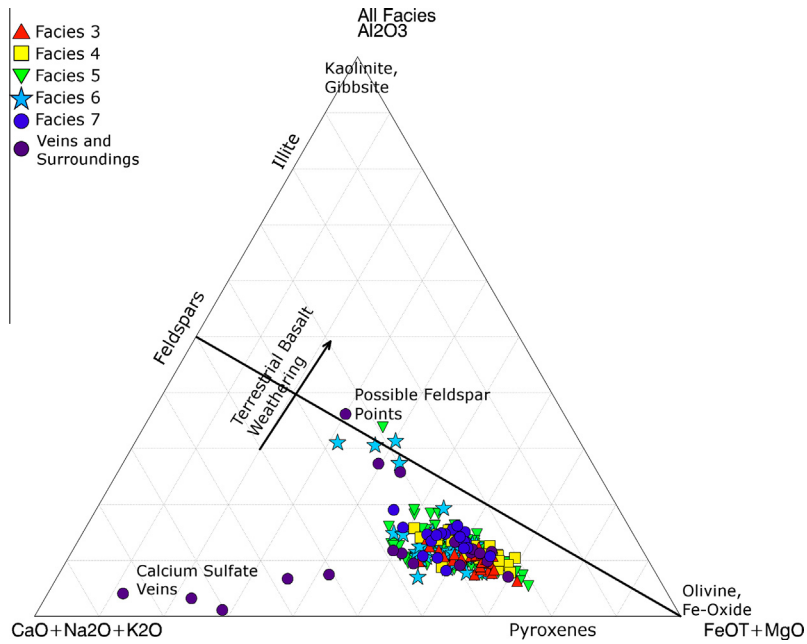
Fig. 12. Shaler points plotted on an A-CNK-FM diagram. Typical terrestrial chemical weathering results in trends toward the upper right of the diagram, above the diagonal line. The only Shaler points that plot above this line are from locations suspected to be enriched in feldspar. Overall there is little indication of chemical weathering at Shaler.

the other cations increases (McLennan et al., 2013; Nesbitt et al., 2009). Points above the line bisecting the $FeO_T + MgO$ corner of the diagram are typically considered to be evidence of alteration. Almost all of the Shaler average points plot well below this line.

The only points above it are those with elevated Al_2O_3 and SiO_2, and these are interpreted to be the result of analyzing individual grains of distinct composition, rather than an indication of changing bulk rock composition because of chemical weathering.
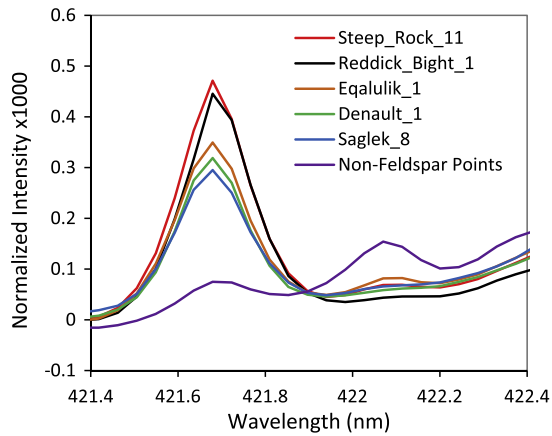
Fig. 13. Average spectra that satisfy the constraints defining possible feldspars ($MgO < 5$ wt.% and $Al_2O_3 > 13$ wt.%) also show elevated Sr at 421.7 nm relative to the average of the other points on these targets. The peak at 422.1 nm is Fe.

Because all of the other analysis points from the Shaler outcrop fall below the line, we consider this to be evidence that the sediment grains that make up the Shaler outcrop have undergone little chemical weathering. This result is consistent with the H ICA scores, which are highest for points that hit soils rather than Shaler rocks, indicating that the rocks do not contain significant amounts of hydrated minerals. Observations from elsewhere in Yellowknife Bay also show little evidence for changes in chemical composition due to chemical weathering (McLennan et al., 2013). This evidence for limited chemical weathering of Shaler detrital components indicates limited chemical weathering in the catchments that sourced Shaler and during fluvial transport. This is likely a consequence of arid and cold climatic conditions coupled with rapid erosion and sediment transport. The presence of sulfate veins indicates that fluids were present post-deposition, but apparently did not affect rock composition because the rocks may have experienced temperatures that were too low, and/or a duration of post-depositional fluid migration that was too short, and/or low water/rock ratios. The low water/rock ratios could be caused by impermeability of the Shaler rocks: water could enter the rocks via fractures to form filled veins, but was unable to permeate the rocks and cause changes to the bulk rock composition.

6.3. Mineral identification and mixing

The small size of the LIBS analysis spot makes it possible to identify spectra that hit single minerals or simple mixtures between minerals (Dyar et al., 2013; Sautter et al., 2014). As noted above, several of the spectra from Shaler stood out in PCA, ICA, and ternary diagrams because of their high alkali and Si contents, suggesting the possible presence of feldspars.

To identify points that are dominated by feldspars, we used single-shot spectra (rather than averaging all spectra at each point). The spectra were restricted to those with low MgO (<5 wt.%), high Al_2O_3 (>13 wt.%), and an Al/Si molar ratio between 0.3 and 0.4. Using these criteria, Saglek point 8, Steep_Rock point 11, Eqalulik point 1, Reddick_Bight point 1, and Denault point 1 all had spectra that indicate the presence of feldspars. Spectra identified in this manner also show elevated Sr (Fig. 13), supporting the inferred presence of feldspars. Estimated abundances for Sr in the putative feldspar points range from 200 to 400 ppm, with an RMSE of 160 ppm (Ollila et al., 2013).
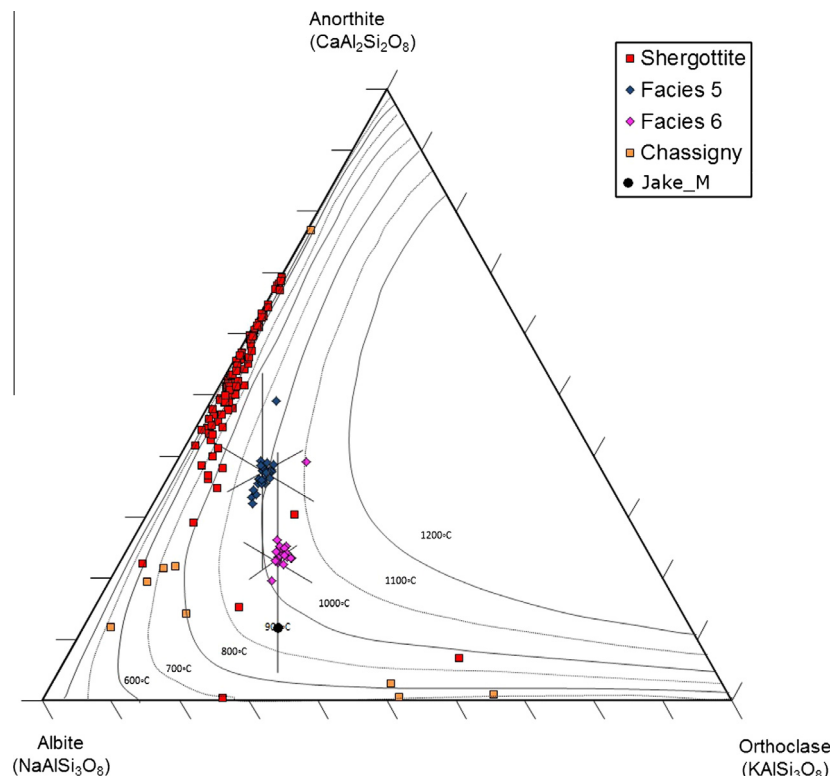
Fig. 14. Feldspathic compositions from selected LIBS shots on Facies 5 and 6, normalized to Fe-free. Representative compositions used are given in Table 3. Feldspar solvi from Drüppel and Lehmann (2009). Shergottite feldspar (maskelynite) compositions from a range of literature sources. Chassigny feldspar (maskelynite) compositions from McCubbin and Nekvasil (2008). Approximate Jake_Matijevic feldspar composition based on CIPW norm values in Stolper et al. (2013). Error bars propagated from RMSE values on PLS1 oxide compositions (Table 3).

In all of the feldspathic points, there is excess FeO_T (up to 13.3 wt.%) that must be normalized out to arrive at a feldspar-like composition. It is possible that this "excess" FeO_T is the result of an Fe-oxide cement similar to that thought to be present at Rocknest (Blaney et al., in press). An alternative explanation of the presence of FeO_T in points that are dominated by feldspathic compositions is that the feldspars may be intergrown with the Fe-oxides. However, if this were the case, FeO_T would correlate with Al_2O_3, K_2O and Na_2O in Shaler single-shot PLS results and ICA scores, which is not observed. We also examined the possibility that the excess FeO_T is an artifact of the PLS1 model used, caused by Si emission lines in the 250–253 nm range, which overlap with some strong

Table 3
Representative Shaler feldspar compositions from LIBS single shots.

Target:	Saglek (Facies 5)	Saglek (Facies 5)	Saglek (Facies 5)	Eqalulik (Facies 6)	Steep_Rock (Facies 6)	Steep_Rock (Facies 6)	
Point:	8	8	8	1	11	11	
Shot:	4	5	15	6	5	8	RMSEP
SiO_2	61.1	65.1	68.1	63.2	61.5	63.8	7.1
TiO_2	0.47	0.45	0.62	0.3	0.3	0.3	0.55
Al_2O_3	17.1	17.5	18	16.1	16.8	16.9	3.7
FeO_T	9.1	8.7	8.2	11.1	11	11.3	4
MgO	2.2	3.2	4.4	0.4	0.7	0.3	3
CaO	4.7	5.1	4.9	3.2	3.6	3.4	3.3
Na_2O	3.6	3.7	3.7	3.9	4.3	4.5	0.7
K_2O	1.5	1.6	1.6	2.4	2.9	2.8	0.9
Total	99.8	105.4	109.5	100.6	101.1	103.3	
Number of ions on the basis of 32O. Normalized Fe free							
Si	11.8	11.8	11.8	12.1	12	12.1	
Al	3.9	3.7	3.6	3.7	3.9	3.8	
Mg	0.6	0.9	1.0	0.1	0.2	0.1	
Na	1.0	1.0	0.9	1.5	1.6	1.7	
Ca	1.3	1.3	1.2	0.7	0.8	0.7	
K	0.4	0.4	0.4	0.6	0.7	0.7	
Or	13.7(±7.2)	13.9(±6.8)	14.8(±6.9)	21.8(±6.5)	23.3(±5.6)	22.5(±5.5)	
Ab	50.1(±4.9)	48.9(±4.8)	48.8(±4.8)	53.8(±4.5)	52.5(±4.1)	54.1(±3.8)	
An	36.2(±17.3)	37.2(±16.1)	36.4(±16.6)	24.4(±20.3)	24.3(±17.7)	23.4(±17.2)	
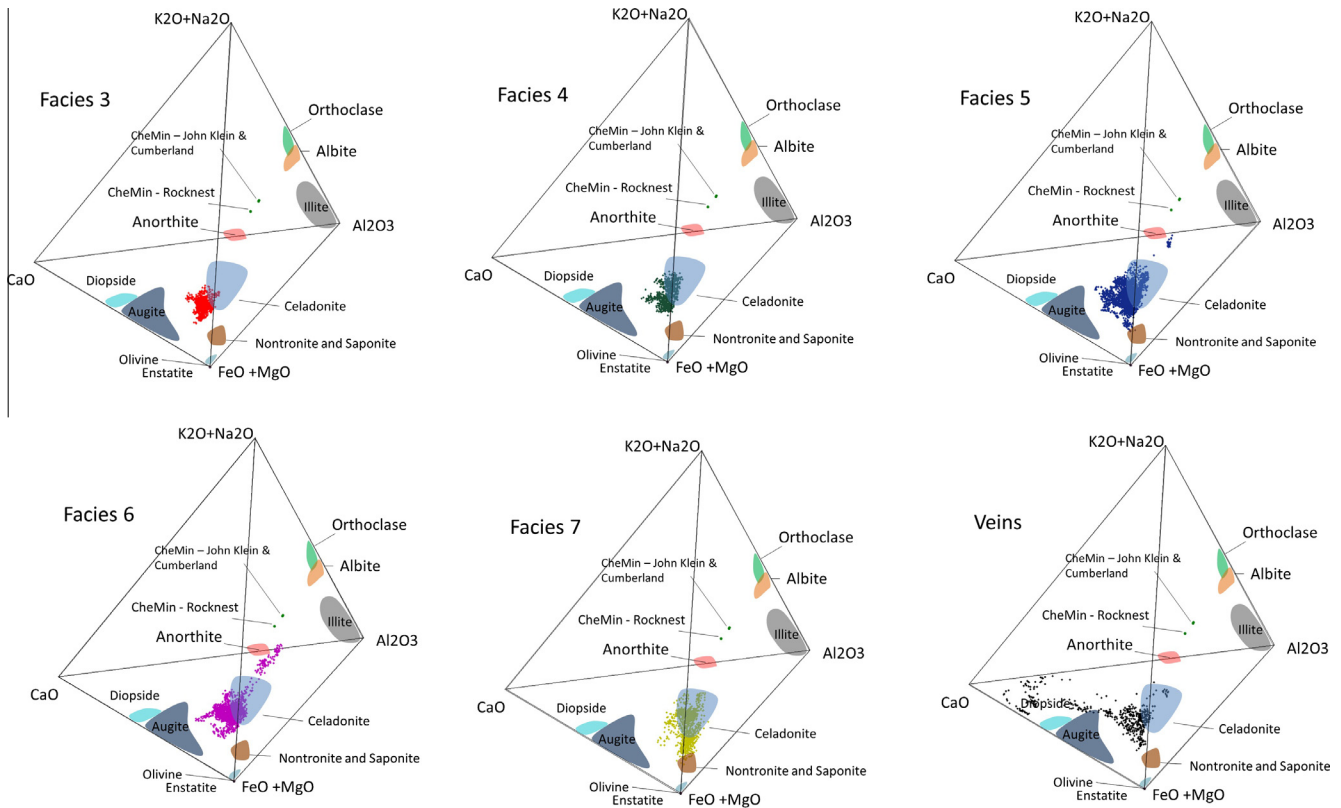
Fig. 15. Tetrahedral diagram of single-shot compositions (wt.% oxide) for the Shaler facies. Note the trend from pyroxene toward feldspars, particularly in Facies 6. Also note the strong trend toward CaO in the vein targets. Feldspathic analyses are most clear in Facies 5 and 6. Fe smectite analyses from Changela and Bridges (2010) and Treiman et al. (1993). CheMin analyses from Vaniman et al. (2013).

Fe lines. However, comparing the strength of the Fe ICA scores for these points with the FeO_T component predicted by PLS1, the scores are consistent with the predicted level of FeO_T, suggesting that the presence of Fe in the feldspathic points is not an artifact.

The compositions of the putative Shaler feldspars plot farther towards the center of the feldspar ternary diagram (Fig. 14) than typically observed in terrestrial feldspars or shergottites, although the 1 RMSE error bars span a wide range (Fig. 14). The stoichiometry of the points (Table 3) is not consistent with a pure feldspar mineral, indicating that there was likely contamination by other minerals within the LIBS spots.

Although a single mineral phase is not responsible for the observed compositions, it is still instructive to examine the calculated feldspar compositions. The compositions of Facies 5 feldspar-rich points cluster around $An_{35}Ab_{50}Or_{15}$ and those of Facies 6 cluster around $An_{25}Ab_{55}Or_{20}$. The compositions, even with the relatively large 1 RMSE error bars, show that the Shaler feldspathic points are more alkaline in composition than most of the feldspar (maskelynite) of the shergottite martian meteorites, which have low orthoclase compositions (e.g. Bridges and Warren, 2006). The alkaline composition of the feldspathic points, compared to the shergottites, suggest that the source region for at least some of the Shaler sediments was an alkaline igneous province. The CIPW-derived plagioclase compositions from the alkaline igneous float rock Jake_Matijevic (Stolper et al., 2013) are approximately $An_{11}Ab_{61}Or_{27}$, which is less anorthitic than the compositions derived from the feldspathic points at Shaler, but still within the 1 RMSE error bars for Facies 6 (Fig. 14).

Single shot results can also be used to search for mixing trends in the analyzed targets. Shaler single shot results in wt.% are plotted on a tetrahedral diagram in Fig. 15, and a mixing trend between the feldspar field (red[1] outline) and the pyroxene field (blue outline) can be seen, most notably in Facies 6. This trend is consistent with the basaltic composition of Shaler, indicating that at the sediment source the physical breakdown of basaltic rocks dominated, and that there was little chemical weathering.

There is little overlap of most of the Shaler shots with nontronite or Fe-rich saponite (orange points near the FeO + MgO vertex of the tetrahedron; Changela and Bridges, 2010; Treiman et al., 1993), suggesting a clay-poor assemblage for most facies. The exceptions to this are Facies 5 and 7 which do overlap Fe-rich smectite compositions somewhat, so the presence of clays in those facies is possible. However, the lack of H signatures stronger than soil suggests that hydrated minerals are not abundant in Shaler.

It is notable that none of the points analyzed at Shaler show evidence of sampling pure FeO, which might be expected if the rocks are cemented by Fe oxides. The PLS1 FeO_T composition of most of the Shaler units is relatively high (>18 wt.%). For comparison, the FeO_T of Rocknest rocks, which were interpreted to contain an iron-oxide cement (Blaney et al., in press), averages 20.6 wt.%, ranging up to 26 wt.% in an individual analysis. However, it should be noted that this is likely an underestimate in the case of Rocknest: on ICA and PCA plots, Rocknest rocks plot with very strong Fe contributions, and the training set used to construct the PLS model has only one sample with FeO_T > 21 wt.%, so the model's ability to extrapolate to higher FeO_T content is limited.

7. Conclusion

ChemCam data from 28 targets at Shaler have allowed a detailed chemical and textural investigation of the well-exposed interbedded sedimentary facies. Facies 1 and 2 were not analyzed

by ChemCam, but the remaining facies all have ChemCam LIBS and RMI data from multiple targets.

Grain size analyses were used to describe the grain size distribution in each target. This was instrumental in defining the sedimentary facies and understanding of the depositional history at the Shaler outcrop. For each of the cross-stratified facies (3, 5, 6 and 7a), grain size analyses indicate that ~97% to 99% of the grains were unresolvable or smaller than coarse sand, consistent with the transport of small grains in migrating bedforms. Resolvable grains in Facies 3 were dominated by coarse sand, while resolvable grains in Facies 5, 6, and 7 were dominated by very coarse sand. A larger fraction of grains could be resolved in Facies 5, varying from 87% to 99%. At least 87% of the area of Facies 5 targets was unresolved, indicating grains smaller than coarse sand, consistent with the transport and entrainment of coarse grains during fluvial deposition. Facies 4 resolvable grains were dominated by granule sized grains. This facies is characterized by recessive weathering and potential desiccation cracks. To reconcile the presence of granule-size grains but a recessive weathering nature, we suggest that perhaps slight differences in grain size distribution or cementing agents controlled the characteristics of this facies. All of the observed area of Facies 7b exhibited grains smaller than coarse sand, consistent with deposition of very fine grains at the toe of a fan.

ChemCam LIBS observations of Facies 3 through Facies 7 at Shaler reveal considerable overlap in chemical composition between the sedimentary facies, and that the heterogeneity within a given facies is generally greater than the variation between the facies. The overlap between facies on PCA and ICA plots (Figs. 5 and 6) suggests a similar average composition. Facies 3 and Facies 7 show a slight deviation from the other facies in the ICA K vs. Na plot (Fig. 6c and d).

The average ChemCam composition of each facies indicates that Facies 4, 5, and 6 are generally similar, while Facies 3 and Facies 7 are distinct, particularly in their K_2O content (Table 2, Fig. 8). Facies 4, 5, and 6 have compositions similar to Sheepbed, but with elevated K_2O and slightly elevated FeO_T. Facies 6 has lower MgO than the other facies, and it has been suggested (Mangold et al., submitted for publication) that it may be related to the Point Lake outcrop, which is also depleted in MgO and has a similar rough surface texture.

Mangold et al. (submitted for publication) suggest that the rough surface texture of Facies 6 and Point Lake may be related to dissolution of Mg-bearing minerals. An alternative explanation for the rough surface texture at Facies 6 is the presence of coarse grains (>2 mm) in an otherwise fine-grained (<0.5 mm) matrix. The coarse grains could be more resistant to erosion than the finer grains, resulting in the observed rough texture. If the coarse grains are feldspars, this would be consistent with the several locations with strong feldspar signatures in the single-shot data for Facies 6. Additional feldspar would reduce the amount of MgO in Facies 6 relative to the other facies by dilution. It would require >20 wt.% of non-MgO-bearing material such as feldspars to be added to Facies 5 to reduce the bulk MgO content to Facies 6 levels.

Facies 3 is depleted in K_2O relative to the other Shaler facies and relative to Sheepbed. It is similar in average composition to the Snake clastic dike (Table 2, Fig. 9), which is interpreted (Grotzinger et al., 2013) to have been injected up through Sheepbed and Gillespie Lake members from a unit that stratigraphically underlies the Sheepbed mudstone in Yellowknife Bay. It is possible that the Snake and Facies 3 represent deposition from a lower-K_2O sediment source region. Alternatively, grain size may also influence the K_2O content: if most of the K_2O occurs in coarse grains, the fine-grained (>99% area composed of grains <0.5 mm) Facies 3 would be relatively depleted. To change the K_2O content of Facies 6 to match that of Facies 3, approximately 15 wt.% of material with

---

[1] For interpretation of color in Fig. 15, the reader is referred to the web version of this article.

the composition of the average Facies 6 feldspar ($An_{25}Ab_{55}Or_{20}$) would need to be removed from Facies 6.

Facies 7 is distinct from the rest of Shaler based on its dark, blocky, resistant appearance. Its elevated K_2O and slightly elevated Na_2O and Al_2O_3 provide additional support in favor of a distinct source.

Facies 7 shows some compositional similarities to float rocks encountered by the rover (Table 2, Fig. 9). These float rocks have two distinct appearances: (1) smooth and stratified, or (2) rough, pitted, and shiny (Fig. 10). Facies 7 exhibits both the shiny, pitted texture (e.g. Chioak, Husky Creek), and evidence of stratification and bedding (Mary_River; Fig. 11). The rough or pitted float rocks generally have lower MgO than Facies 7, although they share the elevated K_2O. The alkaline igneous rock Jake_Matijevic is among the rough-textured float rocks that show similarities to Facies 7. We do not suggest that Facies 7 is igneous, or that Jake_Matijevic is sedimentary in origin. However, they may share a common source region. The low-MgO float rocks could have been transported as ejecta while Facies 7 is composed of sediment derived from the same region. Differences in composition, in particular the higher MgO of Shaler 7 relative to Jake_Matijevic and some other float rocks may be explained by diagenetic processes that the Facies 7 sediment was exposed to during transport, deposition, and cementation.

The layered float rocks are not depleted in MgO, and show significant variation in their K_2O content. Mangold et al. (submitted for publication) grouped the layered float rocks near Yellowknife Bay with the target Bathurst, given its similarly elevated K_2O content. However, Bathurst has lower Na_2O and higher MgO and TiO_2 than Facies 7, and many of the float rocks are more similar to Facies 7 than Bathurst. It is possible that at least some float rocks with compositions similar to Facies 7 were derived from Facies 7, or deposits of a similar nature. This would be consistent with the interpretation that Facies 7 is the edge of the cratered surface terrain type and is more erosion-resistant than other rock types in the Glenelg area: the float rocks could be ejecta from impacts into the cratered surface, or lag from the erosion of the surface.

Facies 7's dark tone, blocky nature, and elevation are all similar to the rocks observed at Rocknest. However, despite these shared characteristics, Rocknest has a significantly stronger Fe signature and weaker Mg signature in its spectra (Fig. 6e and f). Thus, we conclude that Rocknest and Shaler Facies 7 are either unrelated, or that diagenesis at Rocknest has led to depleted MgO and enriched FeO_T, compared to Facies 7.

Although the Fe signature at Shaler is not as strong as that observed at Rocknest, the Shaler facies generally do have slightly elevated FeO_T compared to Sheepbed, and in feldspar-bearing locations, "excess" iron up to 13.3 wt.% is present. The source of this excess iron is not known, but Fe-oxide cement is a possibility, and the presence of an Fe-oxide cement would be consistent with the result of Blaney et al. (in press), who inferred Fe-oxide cement in the nearby Rocknest rocks on the basis of their very high observed iron content (up to 25 wt.%). This is also consistent with the observation from orbit of a hematite ridge at the base of Mt. Sharp which may indicate cementation by Fe-bearing groundwater in the past (Fraeman et al., 2013). None of the analysis points at Shaler indicate that pure Fe-oxide was analyzed, but it is possible that the Fe-oxide is present at the micron-scale within and at the margins of minerals.

The mixing between feldspar and pyroxene on tetrahedral diagrams (Fig. 15) is consistent with basaltic source rocks. The feldspathic points analyzed at Shaler have a more alkaline composition than the maskelynite in basaltic shergottites (Fig. 14), thus we suggest that Shaler sediments were derived from a source area with exposed alkaline basalt. This is consistent with the presence of a potential mugearite in Gale crater (Stolper et al., 2013), and is also broadly consistent with previous observations that indicate a higher average alkali content in landing sites than in Mars meteorites (McSween et al., 2009). The tetrahedral diagram (Fig. 15) also shows the presence of high-Ca veins in targets Denault and Reddick_Bight. These veins stand out from other Shaler targets based on their spectra, and in ICA and PCA plots. Similar veins have been identified in the Sheepbed and Gillespie members of Yellowknife Bay, and are interpreted in those cases to be a late diagenetic product (Grotzinger et al., 2013; Nachon et al., submitted for publication).

It is not possible to determine whether the veins observed at Shaler were formed at the same time as the veins lower in the stratigraphy, but it is likely that they are related. The detection of Ca-sulfate veins in the Glenelg stratigraphy is consistent with detection of sulfates and boxwork features elsewhere in Gale crater from orbit (e.g. Anderson and Bell, 2010; Milliken et al., 2009). Modeling of potential hydrothermal systems in Gale (Schwenzer et al., 2012) predicts the formation of Ca-sulfate, among other minerals, although there is no indication that the veins in Shaler or elsewhere in Glenelg are hydrothermal in nature.

Although high-Ca veins are present, indicating some late diagenetic fluid movement, there is little evidence for changes in chemistry associated with alteration in any of the Shaler facies. Spectra of Shaler rocks do not show a strong H signature compared with soil points (Fig. 6g and h), and in the ternary A-CNK-FM diagram (Fig. 12), there is little indication of chemical weathering. This suggests that the Shaler facies were derived from a source that did not experience much chemical weathering, possibly because of a cold climate, and that after deposition there was little chemical interaction with water, consistent with McLennan et al., (2013). This could be because the Shaler rocks were impermeable, temperatures were too low, wet periods were too brief or some combination of these reasons.

Despite the significant overlap in compositions between the different facies in the Shaler outcrop, our measurements do show three distinct compositions, with differences most apparent in K_2O. Facies 3 has a low K_2O content and appears homogeneous and relatively fine grained, while Facies 7 has an elevated K_2O content, and a distinctive dark and blocky appearance. Facies 4, 5, and 6 have compositions similar to Sheepbed, but with slightly elevated K_2O and FeO_T.

The enrichment in K_2O in Facies 7, as well as in the putative feldspars detected in the other facies, suggest that the Shaler source region was an alkaline igneous province. This is consistent with the interpretation that the Glenelg member of the YKB stratigraphic section is derived from a more alkaline source (McLennan et al., 2013). An alkaline igneous province in the Gale crater region is also consistent with the classification of the rock Jake_Matijevic as an alkali basalt (Stolper et al., 2013). The trend toward more alkaline compositions in the Glenelg member relative to the Sheepbed and Gillespie members would suggest that the Gale crater rim is heterogeneous and that successive episodes of erosion and deposition have transported material with distinct compositions.

To increase the K_2O content of Sheepbed to match the typical Shaler value (~0.8 wt.%), 10–15 wt.% of the Shaler feldspathic composition (Fig. 14; $An_{25-35}Ab_{50-55}Or_{15-20}$) would have to be added to Sheepbed. To increase Sheepbed K_2O to match Facies 7 would require the addition of a very large amount (34–50 wt.%) of the Shaler feldspathic composition, suggesting that a distinct source is more likely.

Alternatively, the elevated K_2O in Shaler compared to the rest of the units in YKB could be related to aqueous transport and enrichment of K. However, it is unlikely that K would be mobilized independent of other elements, and mobilizing K would likely involve the formation of phyllosilicates, which is not indicated in the A-CNK-FM ternary diagram. We therefore favor the simpler

explanation that the feldspars in Shaler are relatively alkaline compared to the maskelynite in shergottites and that the observed chemical variations are the combined result of grain size sorting and multiple sources.

In summary, Shaler is higher in the stratigraphic section than the Sheepbed mudstone, and based on the observed cross-bedding, grain sizes, and facies textures, appears to be the result of fluvial deposition in a higher-energy environment than Sheepbed. The facies are heterogeneous at the scale of the ChemCam LIBS spot, but chemical variations between the facies are still detectable, most notably in the observed K_2O content. Several analyzed locations showed elevated SiO_2, Al_2O_3, Na_2O, and K_2O, suggesting that feldspar grains with greater alkali content than that observed in Mars meteorites were present in the LIBS spots. These locations contained excess FeO_T, suggesting that the grains may be cemented by iron oxides, consistent with the observed presence of Fe-oxides elsewhere in Gale crater. It is possible that some of the variation in composition observed between the facies in Shaler, and between the stratigraphic units in Glenelg, is the result of grain size sorting, but this is likely not the only source of variation. The distinct composition and appearance of Facies 7 indicates a different sediment source. High-Ca veins are observed in Shaler, similar to those observed in other units of the Glenelg stratigraphic section, but the fluids responsible for the vein deposits do not appear to have significantly altered the bulk of the Shaler rocks. The lack of chemical weathering in Shaler is consistent with that observed in Sheepbed, and indicates some combination of low temperature, arid conditions, and rapid erosion and sediment transport.

Acknowledgments

References

Abdi, H., 2003. Partial Least Square Regression (PLS Regression). Sage, Thousand Oaks, CA.

Anderson, R., Bell, J.F., 2010. Geologic mapping and characterization of Gale crater and implications for its potential as a Mars Science Laboratory landing site. Mars J. 5, 76–128. http://dx.doi.org/10.1555/mars.2010.0004.

Blaney, D. et al., 2014. Chemical and textural variability among rocks observed at Rocknest, Gale crater, Mars. J. Geophys. Res., in Press, http://dx.doi.org/10.1002/2013JE004590.

Bridges, J.C., Warren, P.H., 2006. The SNC meteorites: Basaltic igneous processes on Mars. J. Geol. Soc. 163, 229–251. http://dx.doi.org/10.1144/0016-764904-501.

Changela, H.G., Bridges, J.C., 2010. Alteration assemblages in the nakhlites: Variation with depth on Mars. Meteorit. Planet. Sci. 45, 1847–1867. http://dx.doi.org/10.1111/j.1945-5100.2010.01123.x.

Clegg, S.M., Sklute, E., Dyar, M.D., Barefield, J.E., Wiens, R.C., 2009. Multivariate analysis of remote laser-induced breakdown spectroscopy spectra using partial least squares, principal component analysis, and related techniques. Spectrochim. Acta, Part B: At. Spectrosc. 64, 79–88. http://dx.doi.org/10.1016/j.sab.2008.10.045.

Clegg, S.M. et al., 2014. Expansion of the ChemCam calibration database. Lunar Planet. Sci. 45, p. 2378.

Comon, P., 1992. Independent component analysis. High.-Order Stat., 29–38.

Drüppel, K., Lehmann, C., 2009. Fire bombing of the Tell Halaf Museum in Berlin during World War II – Reconstruction of the succession of events based on mineralogical investigations. Eur. J. Mineral. 21, 443–456. http://dx.doi.org/10.1127/0935-1221/2009/0021-1901.

Dudragne, L., Amouroux, A.J., 1998. Time-resolved laser-induced breakdown spectroscopy: Application for qualitative and quantitative detection of fluorine, chlorine, sulfur, and carbon in air. Appl. Spectrosc. 52, 1321–1327.

Dyar, M.D., Bridges, J.C., Wiens, R.C., 2013. Mineralogy at Bradbury landing and Yellowknife Bay, Gale crater, Mars as measured by the ChemCam LIBS. Presented at the Geological Society of America, Denver, CO.

Edgar, L.A., et al., A fluvial sandbody on Mars: Reconstruction of the Shaler outcrop, Gale crater, Mars, Sedimentology, submitted for publication.

Edgett, K.S. et al., 2012. Curiosity's Mars Hand Lens Imager (MAHLI) investigation. Space Sci. Rev. 170, 259–317. http://dx.doi.org/10.1007/s11214-012-9910-4.

Fedo, C.M., Friday, M.E., McGlynn, I.O., McSween, H.Y., 2012. Resolving basaltic sediment characteristics from 2D images using known 3D data: Implications for describing and interpreting the martian surface. Presented at the Geological Society of America, Charlotte, NC, p. 403.

Forni, O. et al., 2013. Chemical variability and trends in ChemCam Mars observations in the first 90 sols using independent component analysis. Lunar Planet. Sci., p. 1262.

Fraeman, A.A. et al., 2013. A hematite-bearing layer in Gale crater, Mars: Mapping and implications for past aqueous conditions. Geology 41, 1103–1106. http://dx.doi.org/10.1130/G34613.1.

Friday, M.E., Fedo, C.M., McGlynn, I.O., McSween, H.Y., 2013. The accuracy of 2D assessment of sediment textures, and application to Mars. Lunar Planet. Sci., p. 2361.

Grotzinger, J.P. et al., 2013. A habitable fluvio-lacustrine environment at Yellowknife Bay, Gale crater, Mars. Science 343. http://dx.doi.org/10.1126/science.1242777.

Jolliffe, I., 2002. Principal Component Analysis. Springer Series in Statistics,, Springer-Verlag, New York.

Langevin, Y. et al., 2013. Processing approaches for optimal science exploitation of the ChemCam Remote Microscopic Imager (RMI) during the first 90 days of curiosity operations. Lunar Planet. Sci., p. 1227.

Le Mouélic, S., Gasnault, O., Herkenhoff, K.E., Bridges, N.T., Langevin, Y., Mangold, N., Maurice, S., Wiens, R.C., Pinet, P., Newsom, H.E., Deen, R.G., Bell III, J.F., Johnson, J.R., Barraclough, B., Blaney, D., DeFlores, L., Maki, J.N., Malin, M.C., Perez, R., Saccoccio, M., 2015. The ChemCam Remote Micro-Imager at Gale crater: Review of the first year on Mars. Icarus 249, 93–107.

Maki, J. et al., 2012. The Mars Science Laboratory engineering cameras. Space Sci. Rev. 170, 77–93. http://dx.doi.org/10.1007/s11214-012-9882-4.

Malin, M.C. et al., 2010. The Mars Science Laboratory (MSL) mast-mounted cameras (Mastcams) flight instruments. Lunar Planet. Sci. 41, p. 1123.

Mangold, N. et al., 2014. Chemical variations of Yellowknife Bay formation sediments analyzed by the Curiosity rover on Mars. J. Geophys. Res.: Planets, submitted for publication.

Maurice, S. et al., 2012. The ChemCam Instrument Suite on the Mars Science Laboratory (MSL) rover: Science objectives and mast unit description. Space Sci. Rev. 170, 95–166. http://dx.doi.org/10.1007/s11214-012-9912-2.

McCubbin, F.M., Nekvasil, H., 2008. Maskelynite-hosted apatite in the Chassigny meteorite: Insights into late-stage magmatic volatile evolution in martian magmas. Am. Mineral. 93, 676–684. http://dx.doi.org/10.2138/am.2008.2558.

McLennan, S.M. et al., 2013. Elemental geochemistry of sedimentary rocks at Yellowknife Bay, Gale crater, Mars. Science 343. http://dx.doi.org/10.1126/science.1244734.

McSween, H.Y., Taylor, G.J., Wyatt, M.B., 2009. Elemental composition of the martian crust. Science 324, 736–739. http://dx.doi.org/10.1126/science.1165871.

Melikechi, N. et al., 2014. Correcting for variable laser-target distances of laser-induced breakdown spectroscopy measurements with ChemCam using emission lines of martian dust spectra. Spectrochim. Acta, Part B: At. Spectrosc. 96, 51–60. http://dx.doi.org/10.1016/j.sab.2014.04.004.

Milliken, R.E. et al., 2009. Clay and sulfate-bearing rocks in a stratigraphic sequence in Gale crater. Lunar Planet. Sci. 40, p. 1479.

Nachon, M. et al., 2014. Calcium sulfate veins characterized by ChemCam Curiosity at Gale crater, Mars. J. Geophys. Res. http://dx.doi.org/10.1002/2013JE004588.

Nesbitt, H.W., Young, G.M., Bosman, S.A., 2009. Major and trace element geochemistry and genesis of supracrustal rocks of the North Spirit Lake Greenstone belt, NW Ontario, Canada. Precambrian Res. 174, 16–34. http://dx.doi.org/10.1016/j.precamres.2009.06.006.

Ollila, A.M. et al., 2013. Trace element geochemistry (Li, Ba, Sr, and Rb) using Curiosity's ChemCam: Early results for Gale crater from Bradbury Landing Site to Rocknest. J. Geophys. Res.: Planets. http://dx.doi.org/10.1002/2013JE004517.

Palucis, M.C. et al., 2013. Origin and evolution of the peace vallis fan system that drains into the curiosity landing area, Gale crater. Lunar Planet. Sci., p. 1607.

Rice, M.S. et al., 2013. Detailed geologic mapping along the Mars Science Laboratory (MSL) curiosity traverse path from Glenelg to Mount Sharp. Lunar Planet. Sci. 44, p. 2892.

Rosipal, R., Krämer, N., 2006. Overview and recent advances in partial least squares. In: Subspace, Latent Structure and Feature Selection. Springer, pp. 34–51.

Sallé, B. et al., 2004. Laser-induced breakdown spectroscopy for Mars surface analysis: Capabilities at stand-off distances and detection of chlorine and sulfur elements. Spectrochim. Acta, Part B: At. Spectrosc. 59, 1413–1422. http://dx.doi.org/10.1016/j.sab.2004.06.006.

Sautter, V. et al., 2014. Igneous mineralogy at Bradbury Rise: The first ChemCam campaign at Gale crater. J. Geophys. Res.: Planets 119, 1–17. http://dx.doi.org/10.1002/2013JE004472.

Schwenzer, S.P. et al., 2012. Gale crater: Formation and post-impact hydrous environments. Planet. Space Sci. 70, 84–95. http://dx.doi.org/10.1016/j.pss.2012.05.014.

Sobron, P., Wang, A., Sobron, F., 2012. Extraction of compositional and hydration information of sulfates from laser-induced plasma spectra recorded under Mars atmospheric conditions—Implications for ChemCam investigations on Curiosity rover. Spectrochim. Acta, Part B: At. Spectrosc. 68, 1–16. http://dx.doi.org/10.1016/j.sab.2012.01.002.

Stolper, E.M. et al., 2013. The petrochemistry of Jake_M: A martian mugearite. Science 341, 4. http://dx.doi.org/10.1126/science.1239463.

Treiman, A.H., Barrett, R.A., Gooding, J.L., 1993. Preterrestrial aqueous alteration of the Lafayette (SNC) meteorite. Meteoritics 28, 86–97. http://dx.doi.org/10.1111/j.1945-5100.1993.tb00251.x.

Vaniman, D.T. et al., 2013. Mineralogy of a mudstone at Yellowknife Bay, Gale crater, Mars. Science. http://dx.doi.org/10.1126/science.1243480.

Wentworth, C.K., 1922. A scale of grade and class terms for clastic sediments. J. Geol. 30, 377–392.

Wiens, R.C. et al., 2012. The ChemCam Instrument Suite on the Mars Science Laboratory (MSL) rover: Body unit and combined system tests. Space Sci. Rev. 170, 167–227. http://dx.doi.org/10.1007/s11214-012-9902-4.

Wiens, R.C. et al., 2013. Pre-flight calibration and initial data processing for the ChemCam laser-induced breakdown spectroscopy instrument on the Mars Science Laboratory rover. Spectrochim. Acta, Part B: At. Spectrosc. 82, 1–27. http://dx.doi.org/10.1016/j.sab.2013.02.003.

Williams, R.M.E. et al., 2013. Martian fluvial conglomerates at Gale crater. Science 340, 1068–1072. http://dx.doi.org/10.1126/science.1237317.

Yingst, R.A., Crumpler, L., Farrand, W.H., Li, R., Cabrol, N.A., Neakrase, L.D., 2008. Morphology and texture of particles along the Spirit rover traverse from sol 450 to sol 745. J. Geophys. Res.: Planets 113. http://dx.doi.org/10.1029/2008JE003179.

Yingst, R.A. et al., 2013. Characteristics of pebble- and cobble-sized clasts along the Curiosity rover traverse from Bradbury Landing to Rocknest. J. Geophys. Res.: Planets 118, 2361–2380. http://dx.doi.org/10.1002/2013JE004435.